

56-P  
HC \$1.50  
MF \$0.75  
ML-TDR-64-161

**EFFECTS OF HYPERVELOCITY IMPACTS ON MATERIALS**

Technical Documentary Report No. ML-TDR-64-161

June, 1964

Air Force Materials Laboratory  
Research and Technology Division  
Air Force Systems Command  
United States Air Force

Project No. 7360, Task No. 736006

(Prepared under Contract No. AF 33(616)-8423 by Technical  
Operations Research, Burlington, Mass.; V. E. Scheraga,  
M. Beran, H. Stevens, R. W. O'Neil, authors)

**tech ops**

## NOTICES

When Government drawings, specifications, or other data are used for any purpose other than in connection with a definitely related Government procurement operation, the United States Government thereby incurs no responsibility nor any obligation whatsoever; and the fact that the Government may have formulated, furnished, or in any way supplied the said drawings, specifications, or other data, is not to be regarded by implication or otherwise as in any manner licensing the holder or any other person or corporation, or conveying any rights or permission to manufacture, use, or sell any patented invention that may in any way be related thereto.

Qualified requesters may obtain copies of this report from the Defense Documentation Center (DDC), (formerly ASTIA), Cameron Station, Bldg. 5, 5010 Duke Street, Alexandria, Virginia, 22314.

This report has been released to the Office of Technical Services, U. S. Department of Commerce, Washington 25, D. C. , for sale to the general public.

Copies of this report should not be returned to the Research and Technology Division, Wright-Patterson Air Force Base, Ohio, unless return is required by security considerations, contractual obligations, or notice on a specific document.

ML-TDR-64-161

**EFFECTS OF HYPERVELOCITY IMPACTS ON MATERIALS**

Technical Documentary Report No. ML-TDR-64-161

June, 1964

Air Force Materials Laboratory  
Research and Technology Division  
Air Force Systems Command  
United States Air Force

Project No. 7360, Task No. 736006

(Prepared under Contract No. AF 33(616)-8423 by Technical  
Operations Research, Burlington, Mass.; V. E. Scherrer,  
M. Beran, H. Stevens, R. W. O'Neil, authors)

## FOREWORD

The hypervelocity facility used for this work was developed by Technical Operations Research under Contract AF 33(616)-8423, Project No. 7360, Task No. 736006, as part of the hypervelocity program of the Physics Division, Air Force Materials Laboratory, Research and Technology Division, Wright-Patterson Air Force Base, Ohio, with Mr. A. K. Hopkins as project engineer.

The authors wish to acknowledge the support of this work by Mr. L. Salzberg, Mr. R. J. Vossler, and Mr. A. Hopkins, of the Physics Division at AFML, and by Dr. F. C. Henriques, President of Technical Operations Research.

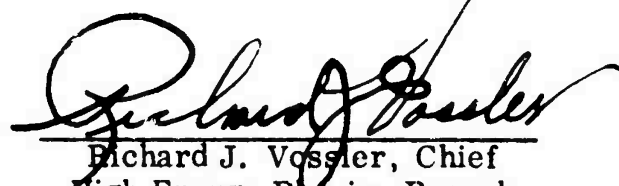
We also acknowledge the aid of Mr. F. Hauser, P. Pearsall, and R. Pelletier in carrying out these experiments.

### ABSTRACT

Reliable diagnostic techniques were developed to measure the mass and velocity of hypervelocity particles projected by an exploding-foil gun. Velocities were increased from 20,000 ft/sec to better than 35,000 ft/sec as a result of improved gun design and modifications to the energy storage system, including the installation of an electrically triggered switching system. The Electro-Optical 6-frame Kerr cell camera was also evaluated.

A program to measure the electrical parameters of the system and to correlate them with photographic data was instituted, and a theoretical model for the partition of impact energy of a hypervelocity particle was begun. Once sufficient data have been taken with the improved particle projection and diagnostic technique, a more comprehensive theoretical program will be instituted.

This technical documentary report has been reviewed and is approved.

A handwritten signature in dark ink, appearing to read "Richard J. Vossler", is written over a horizontal line.

Richard J. Vossler, Chief  
High Energy Physics Branch  
Materials Physics Division  
Air Force Materials Laboratory

## TABLE OF CONTENTS

<u>Chapter</u>	<u>Page</u>
1 INTRODUCTION . . . . .	1
STATEMENT OF PROBLEM . . . . .	1
RESEARCH OBJECTIVES . . . . .	1
BACKGROUND . . . . .	1
2 SUMMARY . . . . .	3
3 HYPERVELOCITY EXPERIMENT FACILITY . . . . .	4
ENERGY STORAGE SYSTEM . . . . .	5
VACUUM SYSTEM . . . . .	7
DIAGNOSTIC EQUIPMENT . . . . .	7
STREAK CAMERA . . . . .	7
FRAMING CAMERA . . . . .	10
BACKLIGHTING SOURCE . . . . .	10
EXPLODING-FOIL GUN . . . . .	11
PRINCIPLE OF OPERATION . . . . .	11
GUN DESIGN DEVELOPMENTS . . . . .	13
RESULTS OF INCREASED GUN EFFICIENCY . . . . .	16
4 DIAGNOSTIC RESEARCH DEVELOPMENTS . . . . .	18
ELECTRO-OPTICAL INSTRUMENTS KERR CELL CAMERA . . . . .	18
SHADOWGRAPH SYSTEM . . . . .	25
DOUBLE-PULSED KERR CELL CAMERA . . . . .	25
STREAK-FRAMING PHOTOGRAPHY . . . . .	26
MEASUREMENT OF PARTICLE MOMENTUM . . . . .	31
ELECTRICAL MEASUREMENTS . . . . .	34
5 THEORETICAL STUDY OF IMPACT OF DISC-SHAPED PARTICLES . . . . .	39
PRELIMINARY CALCULATIONS . . . . .	39
INITIAL IMPACT CALCULATIONS . . . . .	39
ENERGY DISTRIBUTION IN PARTICLE AND TARGET WHEN SHOCK 1 REACHES BACK SURFACE OF PARTICLE . . . . .	44

## TABLE OF CONTENTS (Cont'd.)

<u>Chapter</u>		<u>Page</u>
5	PARTICLE EXPANSION AFTER SHOCK 1 REACHES BACK PART OF PARTICLE . . . . .	45
	REVIEW OF EXISTING THEORIES . . . . .	46
	HYDRODYNAMIC THEORIES . . . . .	46
	EXPLOSIVE-ANALOGY THEORIES . . . . .	47
	RECOMMENDATIONS . . . . .	47
	REFERENCES . . . . .	48

## LIST OF ILLUSTRATIONS

<u>Figure</u>		
1	Equipment Location in Hypervelocity Laboratory . . . . .	4
2	Experimental Area During Installation of Copper Foil Ground Sheet . .	5
3	Schematic Diagrams of Energy Storage System . . . . .	6
4	Energy Storage System . . . . .	8
5	Equipment Installation in Hypervelocity Laboratory . . . . .	9
6	Parallel Plate Transmission Line Installation . . . . .	9
7	Beckman & Whitley Dynafax Framing Camera . . . . .	10
8	Confined Air Arc (Electrical Energy: 1800 joule Time Scale: 5 $\mu$ sec/cm) . . . . .	11
9	First Exploding-Foil Gun . . . . .	12
10	Low-Inductance Modification of Exploding-Foil Gun . . . . .	14
11	First Exploding-Backstrap Gun . . . . .	15
12	Exploding-Backstrap Gun in Present Form . . . . .	17
13	Electro-Optical Kerr Cell Camera Under Test . . . . .	19
14	Kerr Cell Camera Pictures: Side View of Particle in Free Flight (Target impact in lead target was smooth single crater. Velocity was 13,900 ft/sec.) . . . . .	20

# LIST OF ILLUSTRATIONS (Cont'd.)

<u>Figure</u>		<u>Page</u>
15	Kerr Cell Camera Pictures: View of Irregularly Shaped Particle (Particle made a single target impact. Velocity was 16,000 ft/sec.) . .	21
16	Kerr Cell Camera Pictures: View Indicating Limit of Resolution (Small particle debris seen around particle in picture sprinkled area around the crater. Particle velocity was 15,200 ft/sec.) . . . . .	22
17	Kerr Cell Camera Pictures: View of Concentrated Cloud of Particles Moving at Uniform Velocity (Target impact was made by several pieces hitting close together. Velocity was 14,800 ft/sec.) .	23
18	Kerr Cell Camera Pictures: Examples of Shadowgraph Technique (In the first two pictures, a cloud of vapor and small particles can be seen around the principal particle. In the third, the particle is hitting the edge of a lead target.) . . . . .	24
19	Optical System for Shadow Photography . . . . .	25
20	Schematic Diagram of Circuit for Double-Pulsing a Kerr Cell Shutter .	26
21	Schematic Diagram of Basic Optical System Modified for Use with Streak Camera . . . . .	27
22	Method of Measuring Particle Velocity . . . . .	28
23	Method of Taking Velocity Synchronized Streak Picture . . . . .	30
24	Laboratory Installation of Optical System Used with Streak Camera . .	31
25	Streak Framing Pictures of Particles in Flight . . . . .	32
26	Target Recoil Configuration . . . . .	34
27	Gun and Target Chamber for Recoil Studies . . . . .	35
28	Schematic Diagram of Electrical Circuit Used for Measurement of Potential Across the Gun . . . . .	37
29	Pictorial Correlation of Electrical and Photographic Measurements . .	38
30	Plates Before Impact . . . . .	39
31	Plates After Impact . . . . .	40
32	Hugoniot Curves for Copper, Lead, and Aluminum . . . . .	42



## LIST OF TABLES

<u>Table</u>		<u>Page</u>
1	Energy, Pressure, and Density Information for One-Dimensional Aluminum-Lead Impacts . . . . .	43
2	Velocity Information for One-Dimensional Aluminum-Lead Impacts . . . . .	44
3	Energy Distribution When Shock 1 Reaches Back Part of Particle . . . . .	44
4	Energy Distribution In Particle Target System . . . . .	46

## CHAPTER 1

### INTRODUCTION

#### STATEMENT OF PROBLEM

Space vehicles and missiles must be protected from damage or destruction by solid particles moving at high velocities in space. Micrometeoroids can puncture the containing skin of space vehicles, and ballistic missiles are vulnerable to countermeasures employing hypervelocity particles. Before protection devices can be designed for such space vehicles, the effect of hypervelocity impacts on materials must be studied by simulation in the laboratory. The present range of micrometeoroid particle velocities extends from 0 to at least 250,000 ft/sec (72.5 km/sec), the escape velocity of particles from the solar system. Data over this range are of interest not only for hypervelocity impact effects but to better understand existing problems of nuclear and missile warfare.

#### RESEARCH OBJECTIVES

The primary objectives of the work to be performed under Contract AF 33(616)-8423 were to study the exploding-foil gun, to perfect methods of measuring particle mass and velocity, and to provide the supporting research for the development of hypervelocity capabilities at AFML.

#### BACKGROUND

This project was begun in 1961. For this work, Tech/Ops constructed a facility to carry out hypervelocity impact research consisting mainly of an expendable, exploding-foil gun coupled to an electrical energy storage system. The design of this facility was based on the assumption that a high particle velocity was the necessary consequence of high propellant plasma velocity. The exploding-foil guns were capable of accelerating aluminum plasmas to velocities in excess of 250,000 ft/sec. When these same guns were used to propel a light disc-shaped particle, the velocity measured from a uniform, self-luminous plasma front was one fifth that of the free expansion. Since the equilibrium position for a flat disc in a uniform gas flow is such as to present maximum area, the marked difference in the plasma velocity was assumed to be due to its confinement by the small disc; if so, the particle was moving at the measured expansion velocity. A perfect gas seal would be improbable at the very high pressures involved, and naturally there was some evidence of leakage. In front of the assumed particle position, some very low density gas could be seen moving at about twice the velocity of the very dense plasma thought to be propelling the particle. Whenever the particle was shattered in the initial expansion, the front of the plasma expansion became very diffuse, and the velocity was 30% to 40% higher than any recorded for a single particle impact. From this evidence, it seemed our assumption was sound.

---

Manuscript released by authors June, 1964, for publication as a Research and Development Technical Documentary Report.

In the summer of 1963, however, a shadowgraph system was constructed that could penetrate the very bright and nearly opaque plasma around the particle. Our primary assumption as to the position of the particle relative to the plasma front was found to be in error. Particle velocities were 40% to 50% lower than that of the dense plasma front. With the availability of a reliable and accurate particle-velocity measurement technique, it has been possible to double the efficiency of the same basic gun through refinements directed toward better coupling between the plasma and the particle, production of more uniform plane pressure pulses, and elimination of destructive and parasitic mechanisms.

For this reason the work during this latter portion of the project has been directed toward gathering information on the mechanisms of the gun and improving our diagnostic technique so that further increases in particle velocities and reliability of measurement may be obtained. In addition, a preliminary theoretical analysis of impacting disc-shaped particles was developed.

## CHAPTER 2

### SUMMARY

Tech/Ops has constructed a laboratory facility to investigate hypervelocity impact of particles on materials under Contract AF 33(616)-8423 and placed it in operation. This facility includes two banks of 100 kV capacitors, an exploding-foil gun, a vacuum system, a Beckman & Whitley Model 339B continuous writing streak camera, recording electronics, calibrated current loop, and voltage divider circuits for electrical measurements.

An extensive firing program was carried out to measure the mass and velocity of accelerated particles. Pulsed backlighting sources were used to penetrate the dense plasma surrounding the solid particles in this gun. The backlighting source was used with various cameras including the Beckman & Whitley streak camera and the Electro-Optical KFC-600/B six-frame Kerr cell camera. A method was devised for taking simultaneous streak and frame pictures with the Beckman & Whitley streak camera and the velocities obtainable with the exploding-foil gun were increased from 20,000 ft/sec to better than 35,000 ft/sec.

A preliminary theoretical analysis was made of impacting disc-shaped particles. Various existing theories were reviewed for applicability to this work. It is recommended that numerical solutions be sought to explain the cratering process and that attempts be made to obtain experimental data on particle-impact cratering as a function of time to compare with the numerical solutions.

## CHAPTER 3

### HYPERVELOCITY EXPERIMENT FACILITY

The hypervelocity facility consists of a triggered energy storage system, vacuum system, streak and framing cameras for diagnostic measurements, variable output backlighting source, and the expendable exploding-foil gun (Figure 1).

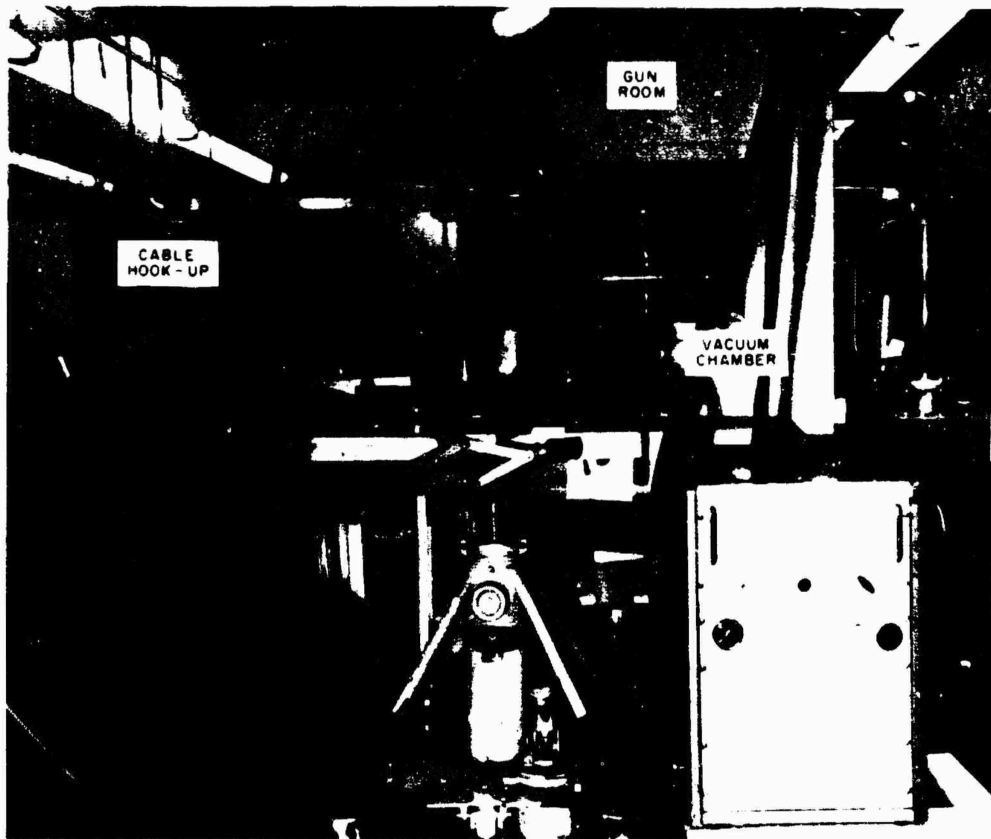


Figure 1. Equipment Location in Hypervelocity Laboratory

Since the gun completely disintegrates when it is fired, a special gun room houses the vacuum chamber and exploding-foil gun to protect the equipment and operating personnel. Also provided in the laboratory are an energy-storage system area, and area for diagnostic equipment, setup space, a dark room, and a shielded control room to facilitate electrical measurements. The entire experimental area is covered with a copper ground plane of 0.005-in. thick copper foil soldered into a continuous sheet (Figure 2) and connected to ground by six copper rods extending approximately 6 ft into the earth. The ground plane is covered with a protective layer of asphalt tile.

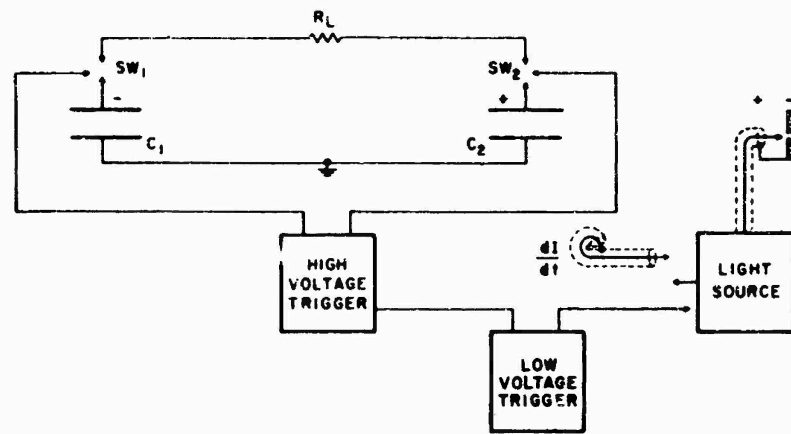


Figure 2. Experimental Area During Installation of Copper Foil Ground Sheet

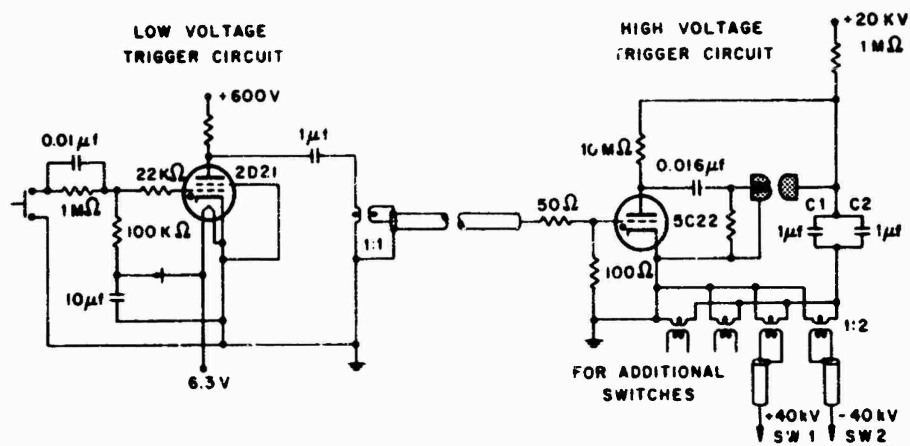
### ENERGY STORAGE SYSTEM

The present energy storage system consists of two banks of capacitors; each bank is a parallel connection of eight  $1\text{-}\mu\text{F}$  capacitors, with each capacitor capable of storing 5000 joules of electrical energy at a potential of 100 kV. The capacitors are guaranteed to last for 1000 shots at full energy when discharged through a load for which the peak-to-peak voltage across the capacitor during discharge does not exceed 180 kV. The capacitors are guaranteed for 10,000 shots or 1 year when charged to no more than 50 kV. At this voltage, the capacitors store 1250 joules each. Since we will fire this facility greatly in excess of 1000 shots we have given the capacitor bank a rating of 10,000 joules at 50 kV.

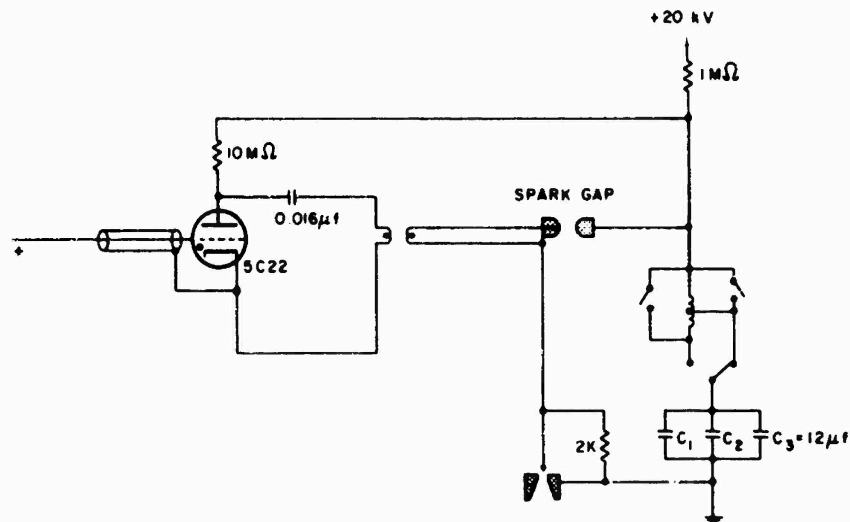
Figure 3 is a schematic diagram of the present electrical circuit: the bank triggering system, a backlighting source, and two  $8\text{-}\mu\text{F}$  capacitor banks connected in series to yield an operating energy of 20,000 joules at 100 kV. This energy is discharged through the hypervelocity gun load transducer,  $R_L$ , by initiating the electronically triggered, reduced-pressure switches, SW. The ringing frequency of this system is 115 kc. The switches are designed to operate from several hundred volts to 60,000 volts with no mechanical modification. Partial evacuation of the switch reduces the dielectric strength of the residual air such that the operating voltage can be changed by adjusting the ambient pressure in the switch with reference to a plot of breakdown voltage vs pressure. If the switch pressure is maintained at  $1\text{-}1/2$  in. to 2 in. Hg greater than the breakdown pressure, a 100-joule trigger pulse will fire the switch with a time jitter of less than  $0.1\text{ }\mu\text{sec}$ .



a. Electrical Circuit of Exploding-Foil Gun Facility



b. Bank Triggering System



c. Backlighting Source

Figure 3. Schematic Diagrams of Energy Storage System

The triggering system, which has been in operation for nearly a year, is capable of firing one to four switches. The output pulse transformer is insulated to withstand a peak voltage of 200 kV between output windings. Reliability has been excellent and the only maintenance performed has been a periodic cleaning of the spark gaps every 500 shots.

Figure 4 shows the energy-storage system in an early stage of development. Figure 4a was photographed while the eight capacitors of one bank were being connected together with the ground plate, before the insulation and top plate were installed. Parallel-plate transmission lines with Mylar insulation between the plates (a good method of connecting capacitors of this type) are used. Figure 4b shows the terminal ends of the two capacitor banks, with the collector plates, Mylar insulation, and reduced pressure switches.

Late in the summer of 1963, the gun room was rotated 90 degrees and moved closer to the capacitor bank (Figure 5) where the two banks were connected into a series arrangement through a low inductance parallel plate transmission line (Figure 6). Several intermediate steps that led up to this modification are discussed with reference to gun performance in the last section of this chapter.

## VACUUM SYSTEM

The vacuum system is a standard 4-in. commercial vacuum system with a mechanical fore pump, a diffusion pump, a gate valve, and a 4-in. pipe. To this system we have added a liquid-nitrogen cold trap near the arc-tube end of the pipe.

## DIAGNOSTIC EQUIPMENT

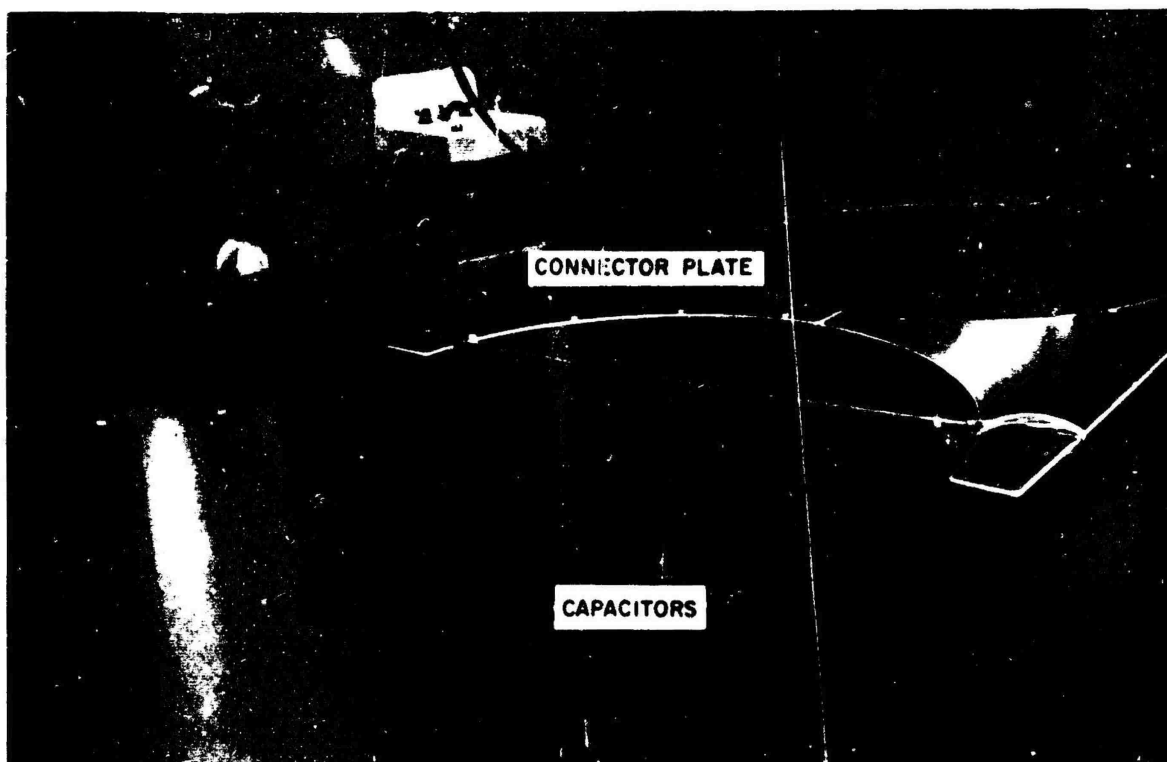
The diagnostic equipment consists of a Beckman & Whitley Model 339B continuous-writing streak camera, a backlighting source, a Beckman & Whitley Dynafax framing camera, a Tektronix Model 551 oscilloscope, and crater-profile tracing equipment. The streak camera and the backlighting source record details of the initial explosion and performance of the exploding-foil gun, and yield measurements from which particle velocities are determined. The Dynafax camera is used for dynamic studies of target impacts, and crater profile tracing equipment is used to study the final results of impact. Relative current measurements recorded by the Model 551 oscilloscope are used to determine circuit damping and ringing frequency.

### STREAK CAMERA

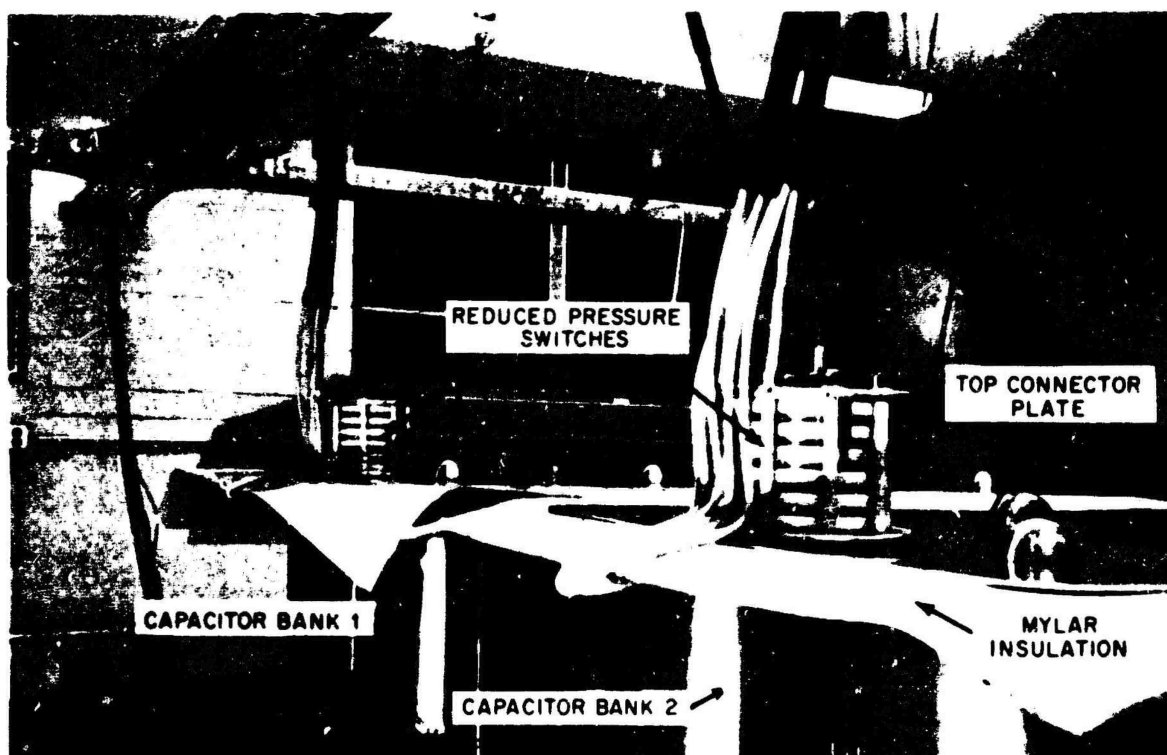
The Beckman & Whitley streak camera (Figure 5) used in this experiment is a research instrument employed in the study of high-speed events. The camera transcribes (on 35 mm film) information which is a variable density record of the illumination falling upon a slit as a function of time. The film is stationary and is swept by the traveling slit image reflected by a rotating mirror. The image of the event is placed on the slit aperture by the objective lens. The internal relay optics are of first-surface mirror construction and give highest resolution to the image reflected onto the curved film track by the rotating mirror in the evacuated body of the camera.

The internal optical system of the camera reduces the image by a factor of 2. A 12-mil slit was used. For this slit width, the time resolution at the maximum writing rate of 9.1 mm/ $\mu$ sec is 16 nsec.





a. Bottom Plate and Storage Capacitors



b. Two Capacitor Banks

Figure 4. Energy Storage System

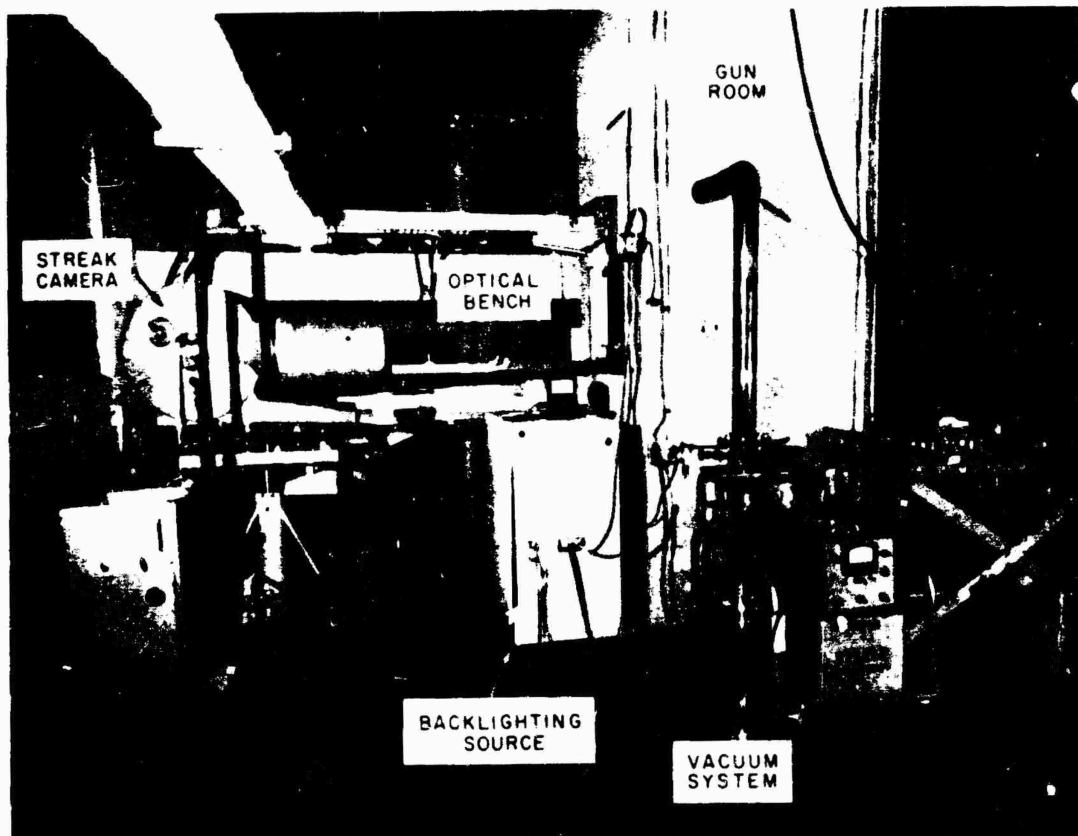


Figure 5. Equipment Installation in Hypervelocity Laboratory

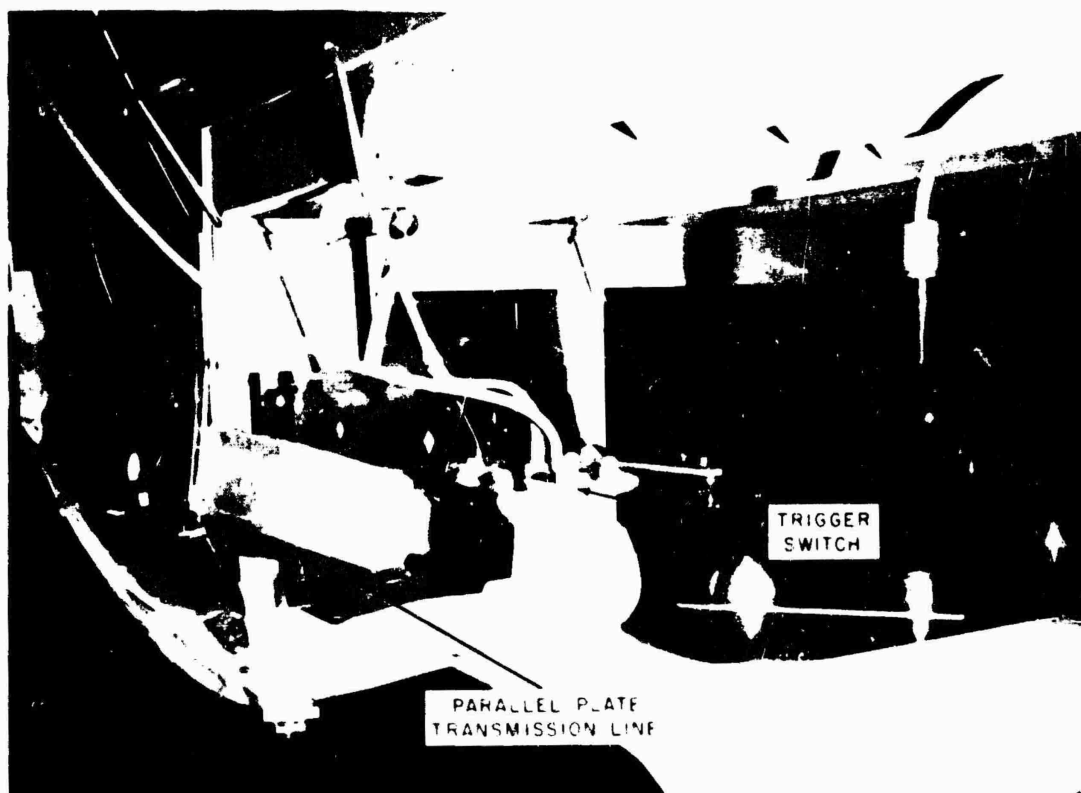


Figure 6. Parallel Plate Transmission Line Installation

The rotating mirror is an aluminized, three-face, optical-quality beryllium mirror driven by turbines. Nitrogen gas drives the turbine to a maximum speed of 2600 rps, giving a maximum writing rate of 9.1 mm/ $\mu$ sec on the f.l.m. Air friction is greatly reduced by evacuating the entire camera housing to a vacuum of 1.5 in. of mercury. The camera is operated from a remote control unit which contains the turbine and shutter controls and an electronic counter. The counter gives a direct read-out of turbine speed in revolutions per second.

#### FRAMING CAMERA

The Beckman & Whitley Dynafax camera (Figure 7) is used primarily for observing slow-moving events associated with target impacts. It has a maximum framing rate of 25,000 fps.

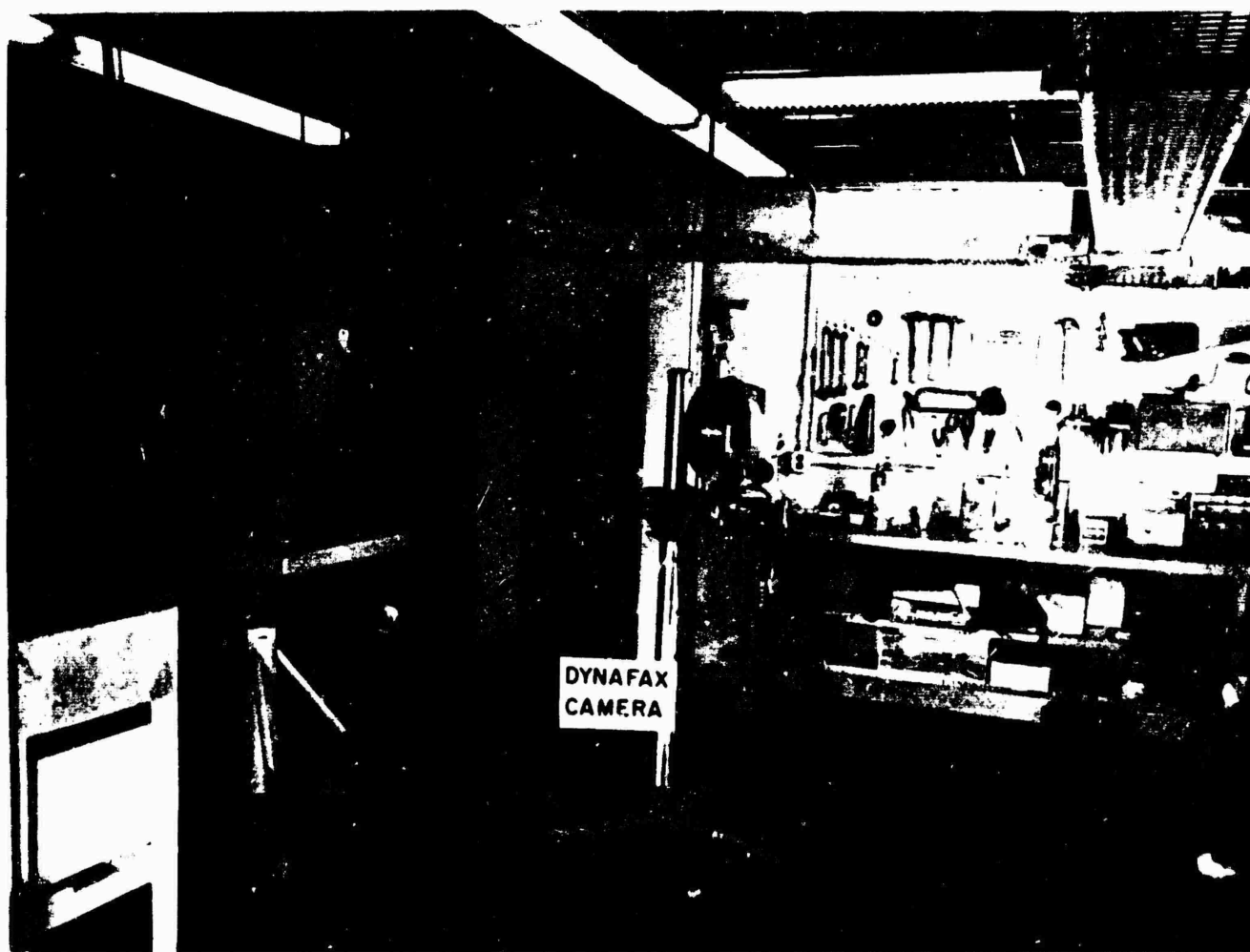


Figure 7. Beckman & Whitley Dynafax Framing Camera

#### BACKLIGHTING SOURCE

To provide the high intensity illumination required by the ultra-high-speed streak camera, a fast rising, short duration electrical discharge system was designed that could be mated to either a confined air arc or an exploding wire.

Since the effective exposure time of the Dynafax framing camera is considerably longer than that of the streak camera, a slower rising, and much longer duration discharge was required.

By choosing a high capacitance and high stored energy, it has been possible to construct a versatile light source that can produce a very intense confined air spark that lasts 30  $\mu$ sec and rises to half intensity in less than 3  $\mu$ sec (Figure 8). By the addition of series inductance, a slower rising discharge is obtained that can provide nearly uniform light for about 5 msec. An exploding wire is the usual transducer for long duration events, but a flashtube can also be used. Proportional taps on the inductor allow easy change to intermediate demands in light duration.

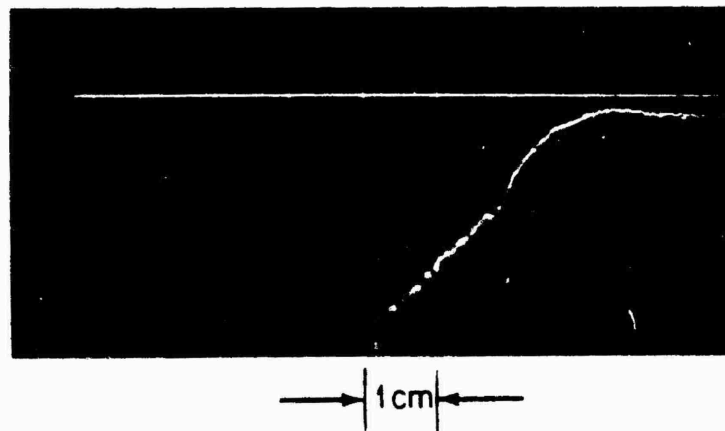


Figure 8. Confined Air Arc (Electrical Energy: 1800 joule Time Scale: 5  $\mu$ sec/cm)

The energy storage system consists of three 12- $\mu$ F, 20-kV capacitors that are discharged through a spark gap switch. If very low jitter is essential, this switch can be positively triggered by a 600-V pulse from a lower voltage thyatron circuit such as a 2D21. If it is desirable, delay circuits can easily be introduced. For less critical timing requirements ( $\pm 1$   $\mu$ sec), a simple antenna or a current loop can be used to synchronize the backlight to the main bank discharge. Schematic diagrams of these two circuits are shown in Figures 3b and 3c.

## EXPLODING-FOIL GUN

### PRINCIPLE OF OPERATION

The "gun" used in these experiments consists of an electrically exploded foil as the "explosive charge," a solid plastic as the "breech," and a cylindrical tube as the "barrel." The end of the barrel is housed in a vacuum chamber containing the target.

In operation, the foil is placed in the breech area of the gun and the gun is initiated by an electrical discharge from the energy storage system. The electrical explosion is separated from the gun barrel and vacuum chamber by a diaphragm (rupture disc) which

contains the explosion for a time about equal to the effective discharge time of the electrical circuit. The diaphragm ruptures forming a disc-shaped particle (projectile) which is intended to fit the barrel very tightly and provide a good gas seal. The hot propellant gas expands and expels the particle from the barrel where it impacts against the target. Exploding-foil guns capable of accelerating aluminum plasmas to velocities over 250,000 ft/sec were developed (Figure 9).

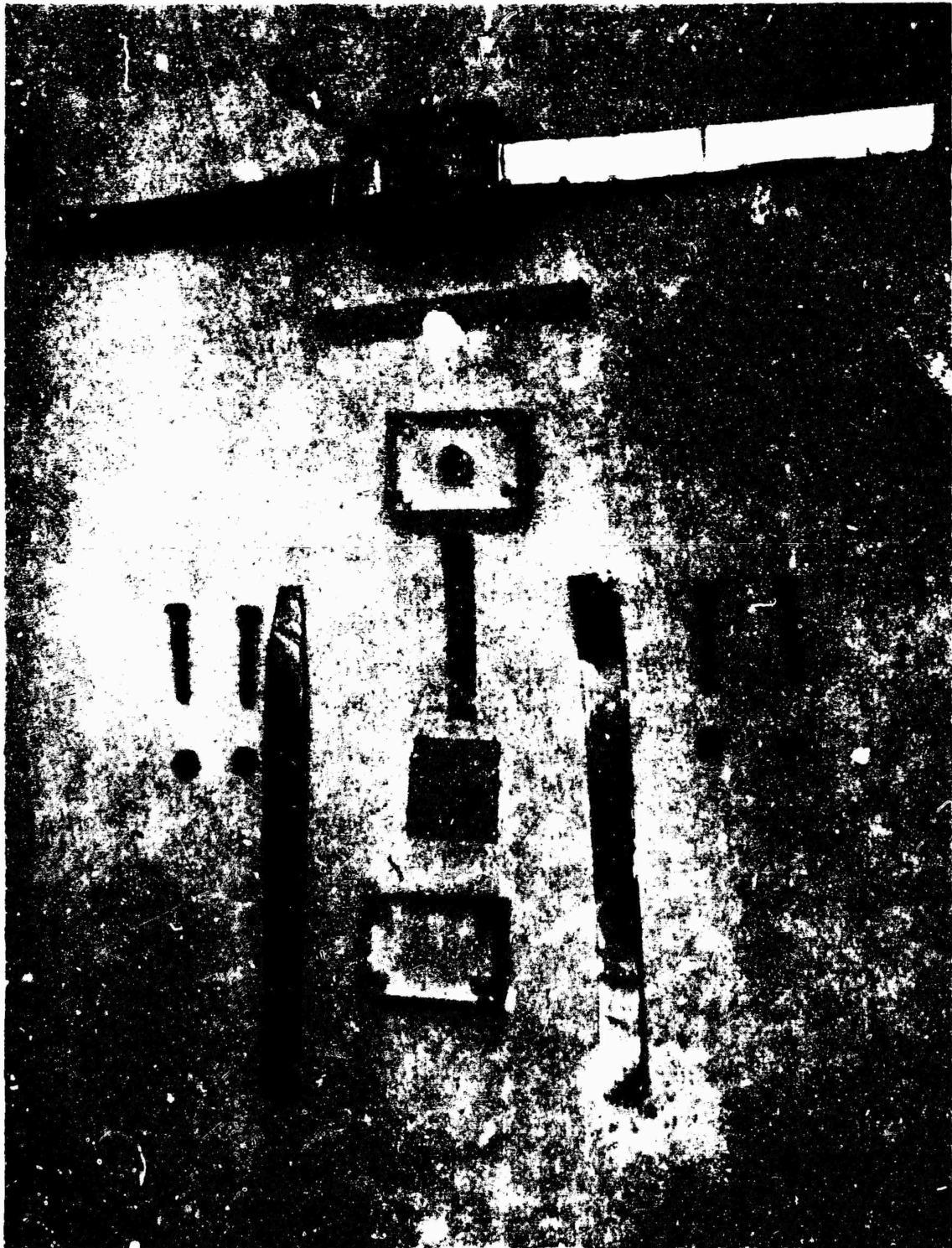


Figure 9. First Exploding-Foil Gun

## GUN DESIGN DEVELOPMENTS

Prior to July 1963, the primary assumption underlying the work done in this experiment was that a high particle velocity was the necessary consequence of high propellant plasma velocity. When the exploding-foil guns developed to implement this idea were used to propel a light disc-shaped particle, the velocity measured from a uniform, self-luminous plasma front was one fifth that of the free expansion. To measure the velocities, the exploding-foil gun was arranged so that the center line of the gun barrel, breech, and target was focused on the slit of the streak camera by the objective lens. Thus, we could observe the initial, contained-foil explosion, the rupture of the particle disc, and the expansion of the hot propellant gas.

When used in this manner, the streak camera did not see the accelerated particle in the gun, but rather recorded the position of the propellant plasma as a continuous function of time. Since the equilibrium position for a flat disc in a uniform gas flow is such as to present maximum area, the marked difference in the plasma velocity was assumed to be due to its confinement by the small disc; if so, the particle was moving at the measured expansion velocity. A perfect gas seal would be improbable at the very high pressures involved, and naturally there was some evidence of leakage. In front of the assumed particle position, some very low density gas could be seen moving at about twice the velocity of the very dense plasma thought to be propelling the particle. Whenever the particle was shattered in the initial expansion, the front of the plasma expansion became very diffuse, and its velocity was 30% to 40% higher than any recorded for a single particle impact. From this evidence, it seemed that our assumption was sound.

In the summer of 1963, however, a shadowgraph system was constructed that could penetrate the very bright and nearly opaque plasma around the particle. Our primary assumption as to the position of the particle relative to the plasma front was found to be in error. Particle velocities were 40% to 50% lower than that of the dense plasma front. With the availability of a reliable and accurate particle-velocity measurement technique, it has been possible to double the efficiency of the same basic gun through refinements directed toward better coupling between the plasma and the particle, production of more uniform plane pressure pulses, and elimination of destructive and parasitic mechanisms. The improved gun is shown in Figure 10. To increase the amount of energy coupled to the projected particle, several new approaches were tried, and a blending of three of these led to considerable success.

The first step was to increase the amount of energy deposited before the particle shears out. This was done by minimizing the total circuit inductance to gain a higher discharge frequency. Since this also sharpened the peak of the initial pressure pulse, particle breakup became a very serious problem. This led to the logical second step of designing a more suitable transducer for the electrical discharge circuit.

Since the very high plasma velocities were proof of the basic soundness of the exploding-foil technique, the technique was not altered drastically. Seemingly small changes in the foil dimension and orientation, however, made significant improvements in the maximum velocities and the percentage of single-particle impacts. Several independent variations led to an exploding-foil geometry in which the foil was doubled back over an insulator, forming both an exploding backstrap and a minimum-inductance gun configuration (Figure 11). (The benefits of this geometry will be discussed later.) To maximize the potential of this new geometry, new high-strength insulators and gun materials were tried that could better withstand the high stress conditions inside the gun. The new materials and backstrap geometry enabled us to punch out 1/8-in. diameter particles from 0.010-in. Mylar without elaborate preparation. Since better circuit



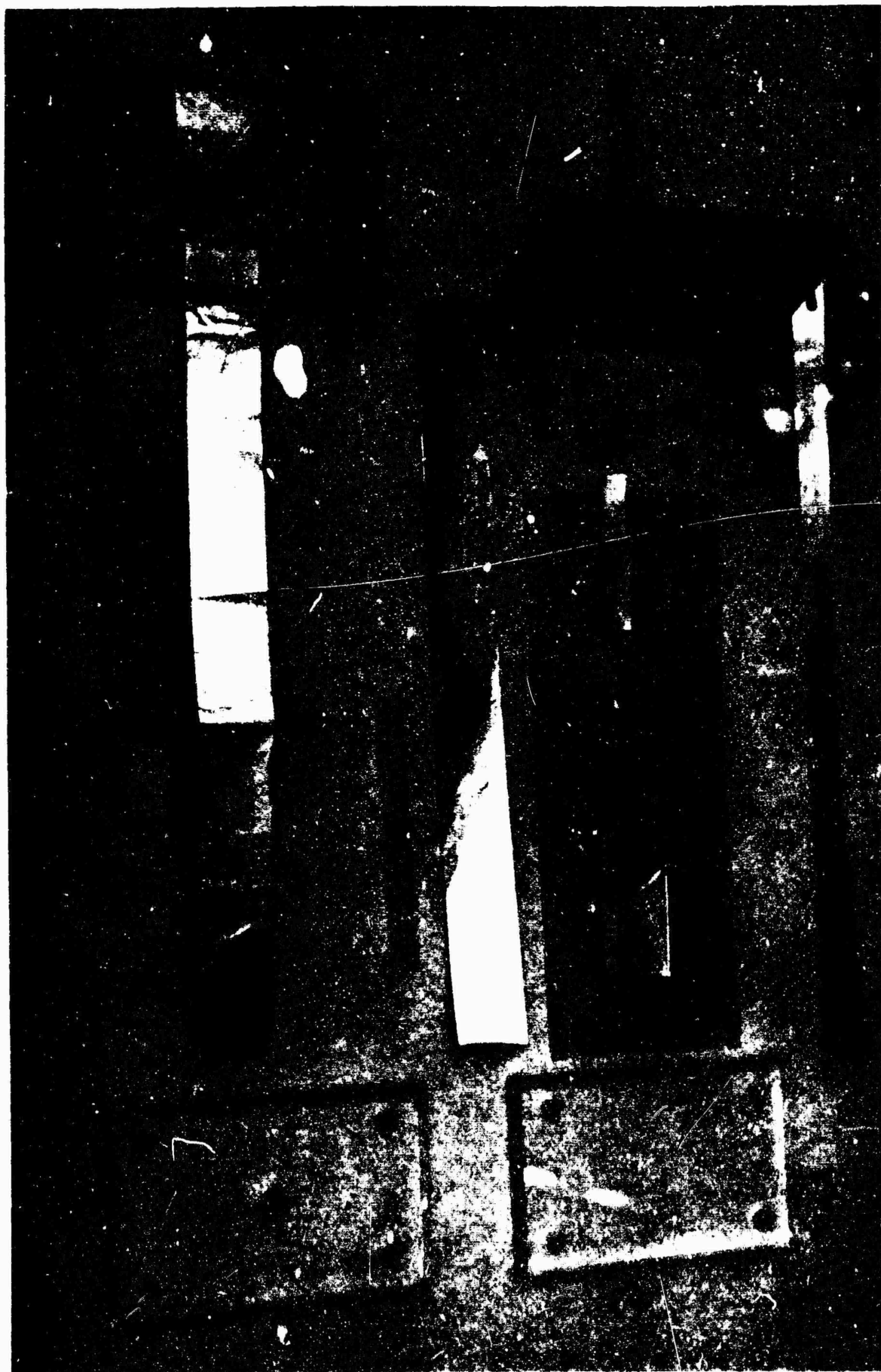


Figure 10. Low-Inductance Modification of Exploding-Foil Gun



Figure 11. First Exploding-Backstrap Gun

matching could be achieved with the smaller area foils, the particle diameter-to-length ratio was improved, and any irregularities were reduced by a factor of 4. The 1/8-in. diameter particles were used for most of the work. Any improvements have been shown to be generally applicable to all gun sizes, but reliability was considerably lower with larger diameter particles. In the course of changing over to the smaller diameters, barrel lengths longer than 1/2 in. were found to have little beneficial effect. Such a short barrel could be machined very accurately in a larger block and, with this geometry, it was quite easy to introduce a steel plate between the gun and the vacuum chamber to eliminate nearly all the late-time gun debris.



## RESULTS OF INCREASED GUN EFFICIENCY

By blending higher power delivery to a new multiple-purpose transducer in a geometrically simple gun, made with commercially available, high-strength materials, single-particle velocities were raised from an average close to 20,000 ft/sec to a high of 36,500 ft/sec in a period of 4 months.

Early in August, the highest velocity recorded by the then new discrimination technique was less than 23,000 ft/sec. The discharge system was a single 8- $\mu$ F capacitor bank operated at 50 kV; the discharge frequency was 60 kc to 65 kc. Since, under certain conditions, the amount of energy a resistive load can absorb increases with the voltage gradient, another bank of 8- $\mu$ F capacitors was connected in series with the existing bank through long cables. The discharge frequency dropped to 57 kc, and although the operating voltage was increased to 100 kV and the available energy doubled, the highest velocity recorded was 22,000 ft/sec. This seemed to indicate that the circuit inductance was too high to take advantage of the energy increase. A single bank was then equipped with a low-inductance discharge circuit that rang at 150 kc. With the same guns used previously, velocities averaged 25,000 ft/sec, and a high of 26,500 ft/sec was recorded for a single impact. For several shots, bank voltage was increased to 70 kV, and several shots yielded velocities of 29,000 ft/sec. After several weeks of experimenting with gun design, a low-inductance parallel-plate transmission line was installed to connect two 8- $\mu$ F capacitor banks in series, yielding an available energy of 20,000 joules at 100 kV. The discharge frequency was 115 kc.

Several significant improvements followed in gun design. For some time it had been known that poor plasma confinement would drastically reduce the efficiency of the gun, but whenever materials of high-impact strength were used to maintain close spacing, the particle disintegrated. Reflected shocks in and around the particle were thought to be the cause of its destruction. To reduce these shock effects, the previously mentioned exploding-backstrap geometry was tried in the hope that the shocks produced by the two branches of the foil would cancel behind the particle and bring the material there to a high state of compression during the breakout time. In the first guns, four sheets of 0.010-in. Mylar were used for electrical insulation. Normal to its surface, Mylar has fairly poor impact strength, and the multiple layer insulator tends to break up the shock profiles from the two foil branches such that they do not cancel very efficiently. The introduction of a one piece, high-strength insulator made of laminated fiberglass increased the single particle impact percentage to greater than 70% and brought velocities up to a consistent 29,000+ ft/sec. In general, the thinner the insulator, the better the gun performance, but insulation demands limit minimum thickness to 1/32 in. at 100 kV.

Laminated fiberglass has a good degree of planarity, and it is very easily fabricated. A slot was made some distance from the edge of the insulator, and the foil was brought through it. Specially-made spacers of the same material were fabricated to maintain parallel faces and to confine the plasma expansion. In addition, a 1/16-in. thick piece was laminated to the breakout surface of the lucite block in which the gun barrel was reamed. Both were then reamed as a unit. With these improvements (Figure 12), it was possible to fire 1/8-in. diameter, 0.010-in. thick Mylar projectiles to 33,000 ft/sec in a fairly regular fashion. These guns used aluminum foils 5 mm wide and 11 mm long and 0.001-in. thick.

By using foils 0.0007-in. and 0.00025-in. thick with the same area, it was possible to project a single particle to 36,500 ft/sec. Reliability with the thinner foil was quite poor due to very small nonuniformities that produce a nonplanar pressure pulse. Better ways of controlling foil uniformity are being investigated.



Figure 12. Exploding-Backstrap Gun in Present Form

Nearly 1500 shots were fired in this contract period, and many avenues of approach were investigated. Significant success was made in increasing particle velocity from about 20,000 ft/sec to better than 35,000 ft/sec. As more information is gathered on the mechanisms of the gun, further increases in velocity and reliability will be possible.

## CHAPTER 4

### DIAGNOSTIC RESEARCH DEVELOPMENTS

The coupling of energy from a large pulsed power system to a load transducer with time-dependent characteristics is a complicated phenomenon. Therefore careful diagnostic experiments offer the most promising method of understanding the system. The most effective diagnostics for the exploding-foil gun are measurements of electrical input to the gun, and high-speed photographic studies of the resulting explosion and particle acceleration.

#### ELECTRO-OPTICAL INSTRUMENTS KERR CELL CAMERA

As part of a program of diagnostic studies of the exploding-foil gun, we investigated the use of a multiple frame Kerr cell camera, the KFC-600/B, produced by Electro-Optical Instruments, Inc. (EOI). This camera uses a special prism to split the optical beam inside the camera into six components. Each component passes through a Kerr cell shutter and film holder. Six frames are taken with an exposure time per frame of 10 nsec. The time between frames is adjustable from 10 nsec to 5  $\mu$ sec.

We obtained a model of this camera on loan for tests with our experiment. Figure 13 shows the camera setup with our experiment. A careful examination of the camera revealed that a telecentric shadowgraph optical system (described later) cannot be used with this camera because the beam splitter is located behind the objective lens in such a position that this geometry is not possible. In fact, we have not been able to design any optical system, with up to five lenses, that will permit the aperture arrangement necessary for the geometrical discrimination of light from propellant gases. One might, with considerable effort, be able to discriminate with this camera, just on the basis of wavelength. For example, laser light with very narrow bandpass filters might be a possible answer. However, we feel that the lighting arrangement shown in Figure 19 is important to the success of this type of photography, and we propose the shadowgraph method described later in this chapter.

A method of using the KFC-600/B camera was found that permitted taking good pictures in the particle free-flight region. Discrimination against light from hot propellant gas was obtained by using a large area foil, which was exploded with a 7200 joule pulsed energy source. The foil to be exploded was the size of the region of interest in the picture, and it was placed as close as possible behind the gun. Discrimination against plasma was obtained on the basis of the relative intensity of light sources.

Figure 14 shows a typical example of the performance of this arrangement. The camera is capable of taking six frames. One frame was used to measure bleed through, one frame used a polaroid film, and one frame missed the particle. In Figure 14 we show frames 3, 5, and 6. The exposure time per frame was 10 nsec; the interframe time was 1.2  $\mu$ sec. In frame 3 we see the particle partly obscured by plasma. In frames 5 and 6, a clear backlighted picture of the particle is shown. These pictures show that the particle came out of the gun barrel edgewise. The original dimensions of the particles shown in this section were 0.250 in. in diameter and 0.010 in. thick.

Figure 15 shows three frames from a similar shot. In this case, the particle velocity was higher, but the shape of the particle was more irregular. However, the orientation of the particle was more desirable than in the previous example.

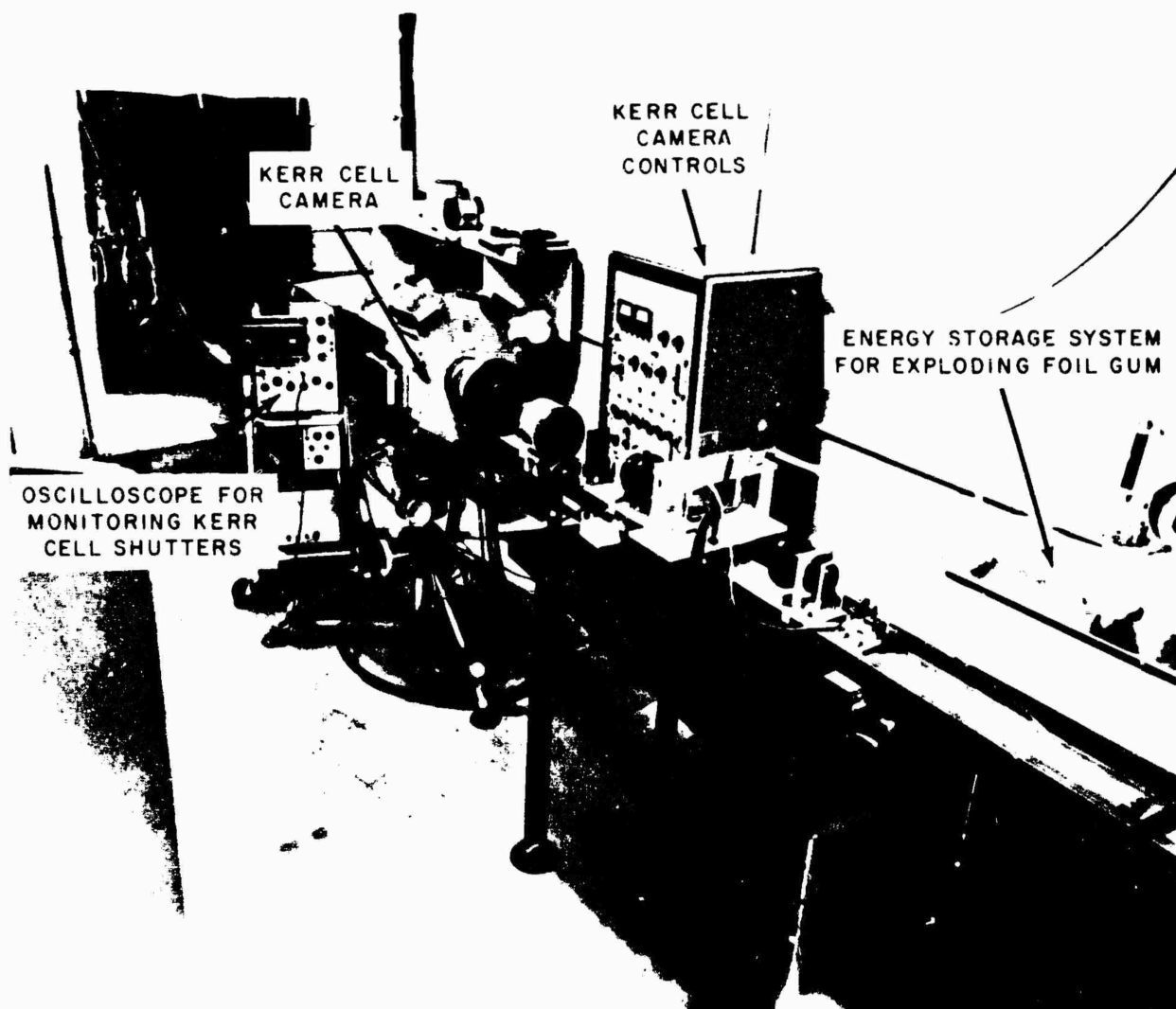


Figure 13. Electro-Optical Kerr Cell Camera Under Test

The resolution that is possible with this method is illustrated in Figure 16. As before, three selected frames are shown. In the last frame a small cloud of very small particles is visible and it is fairly well resolved.

Figure 17 illustrates the photography showing small bits of debris around the principal particle. These smaller pieces seem to be ablating and forming a gaseous cloud.

It was pointed out above that a collimated backlighting system cannot be used with the KFC-600/B camera. However, it is possible to angle the camera so that a single frame picture can be taken. Primarily to illustrate the advantage of collimated backlighting, we fired several shots with such an arrangement. The results of these tests are shown in Figure 18.

The three pictures taken with the KFC-600/B camera and the basic optical system by using only one prism face and Kerr cell were printed from a negative obtained by photographing the polaroid originals and some detail is lost, but quality and depth of field can be seen to be superior to the extended field backlighting which must be used for more than one frame with the EOI six-frame camera.

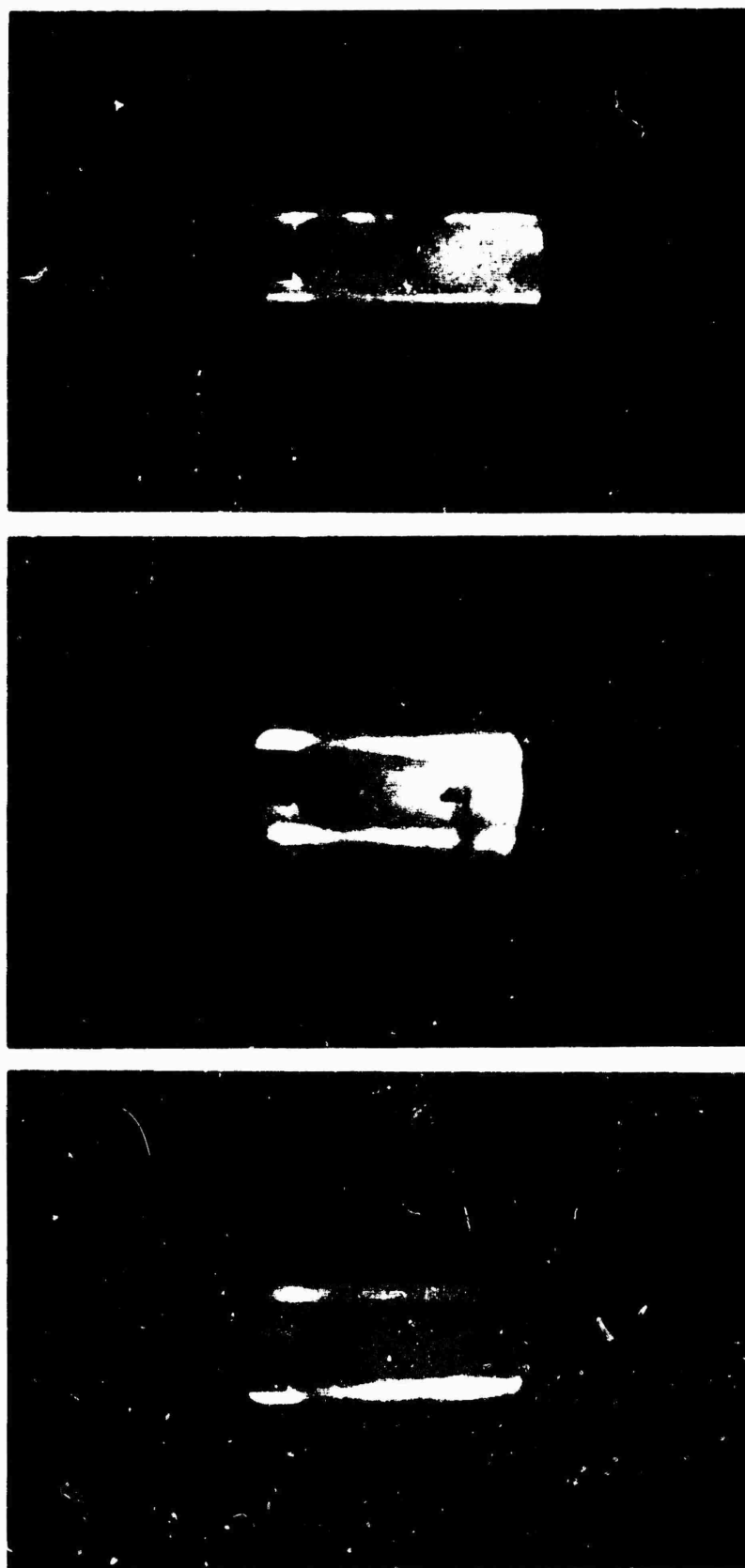


**Figure 14.** Kerr Cell Camera Pictures: Side View of Particle in Free Flight (Target impact in lead target was smooth single crater. Velocity was 13,900 ft/sec.)

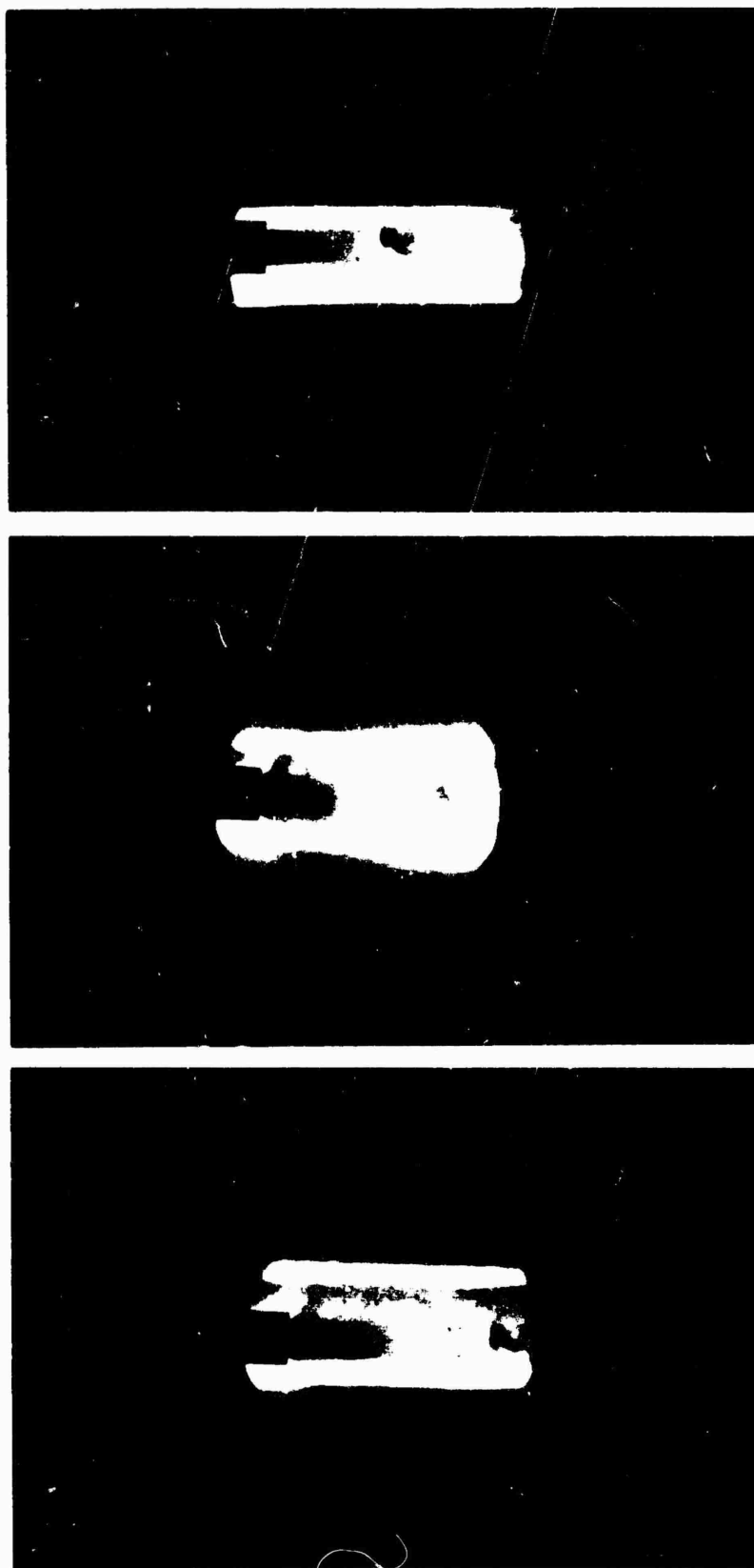
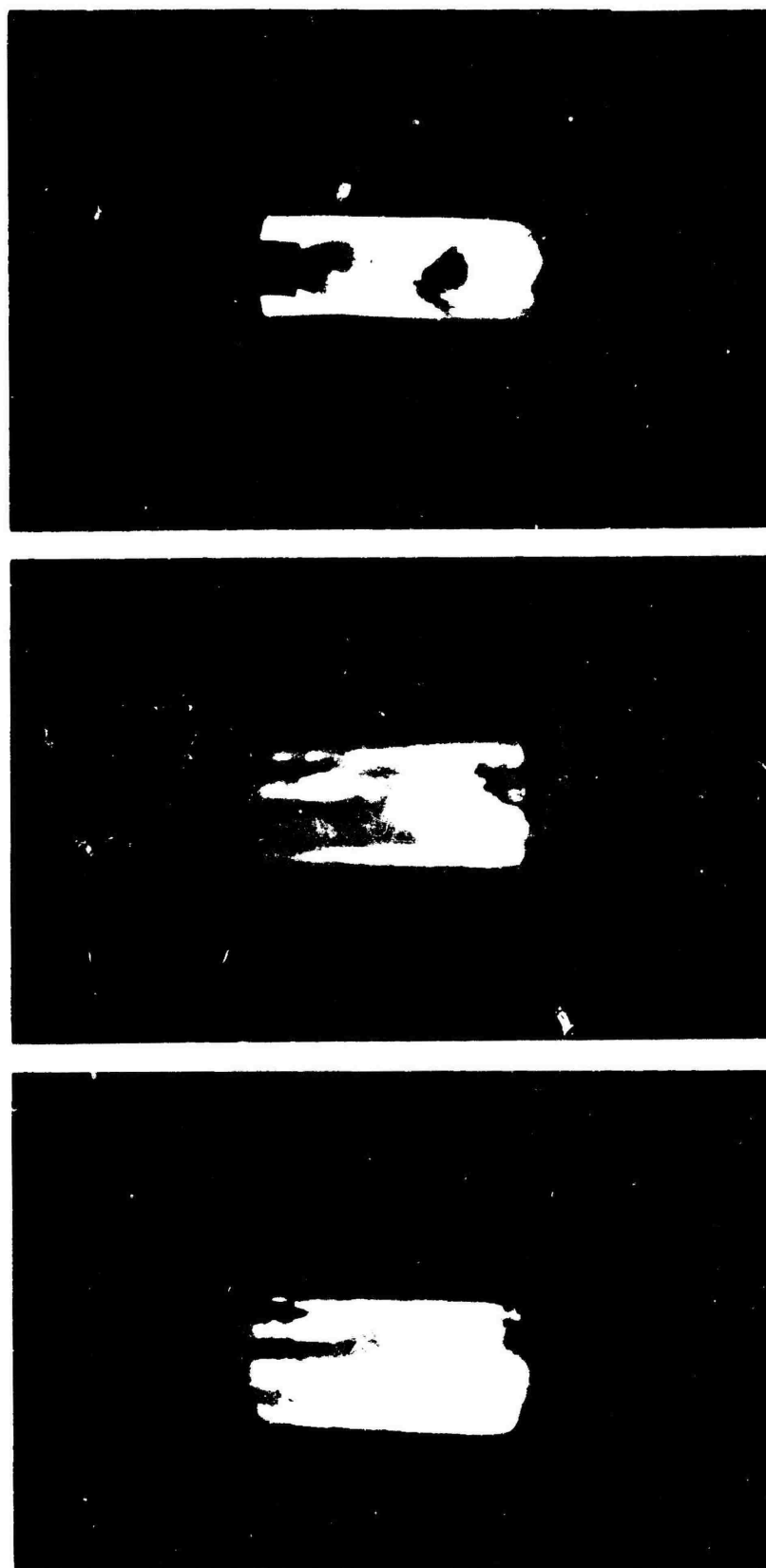


Figure 15. Kerr Cell Camera Pictures: View of Irregularly Shaped Particle (Particle made a single target impact. Velocity was 16,000 ft/sec.)



**Figure 16.** Kerr Cell Camera Pictures: View Indicating Limit of Resolution (Small particle debris seen around particle in picture sprinkled area around the crater. Particle velocity was 15,200 ft/sec.)

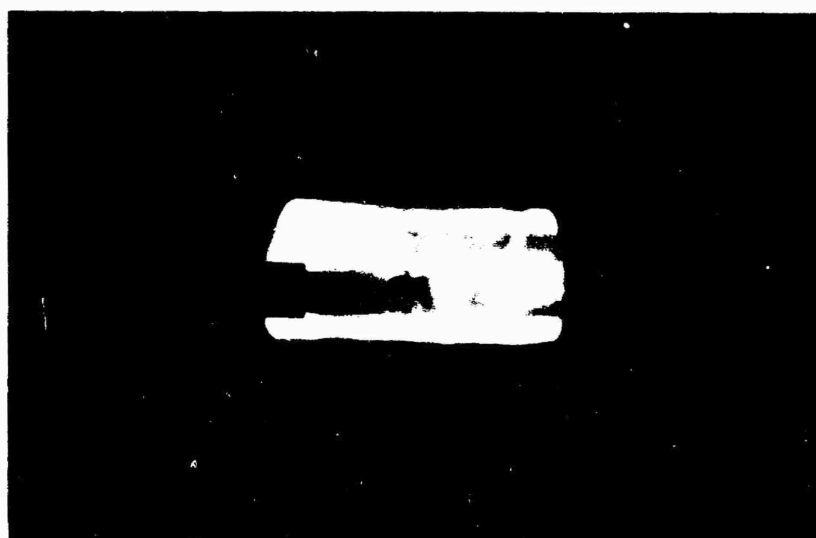
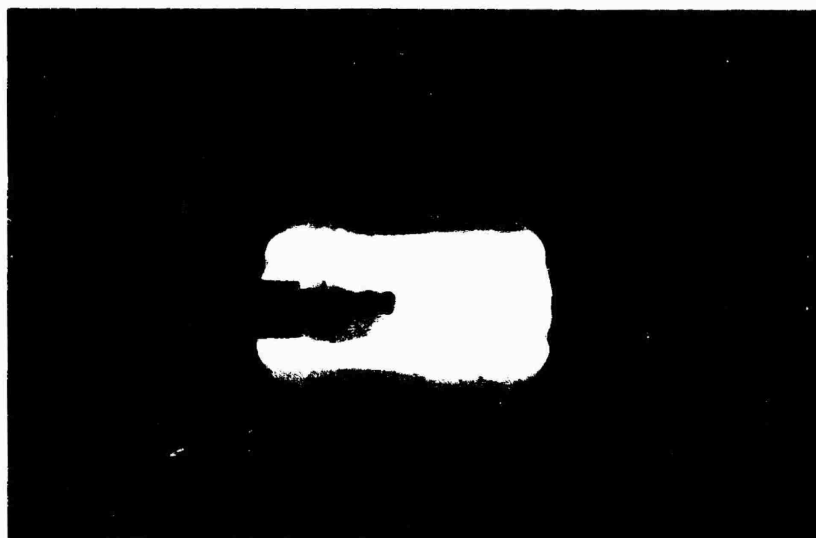
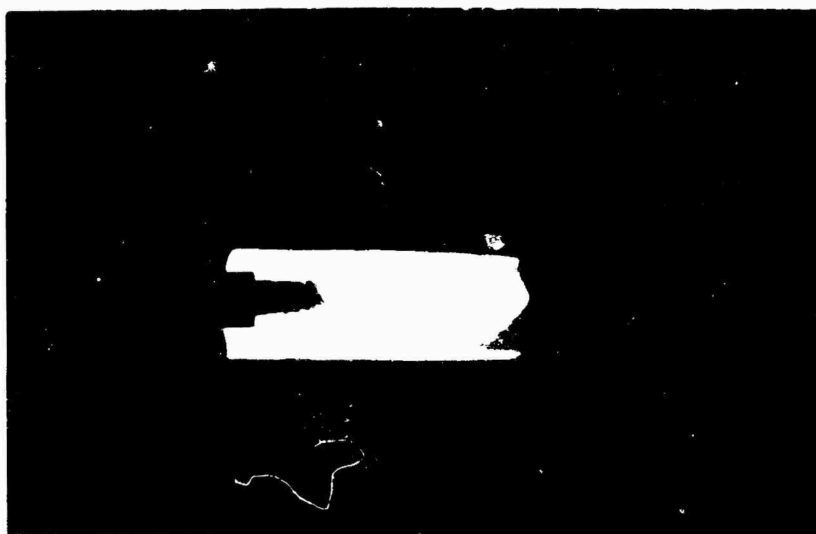
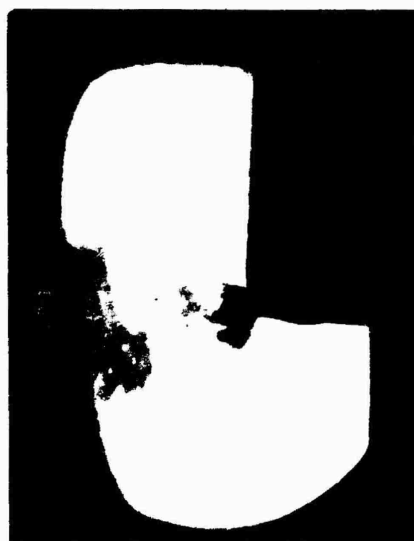
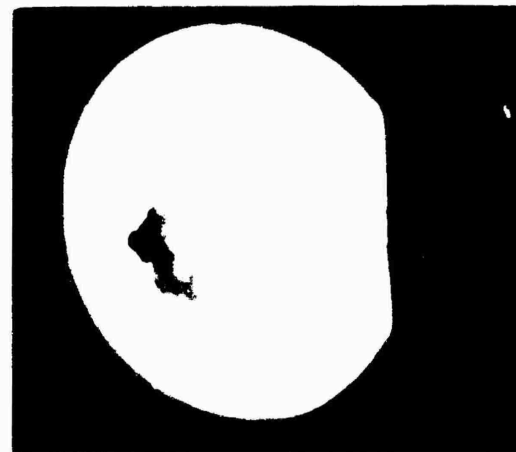


Figure 17. Kerr Cell Camera Pictures: View of Concentrated Cloud of Particles Moving at Uniform Velocity (Target impact was made by several pieces hitting close together. Velocity was 14,800 ft/sec.)





**Figure 18. Kerr Cell Camera Pictures: Examples of Shadowgraph Technique (In the first two pictures, a cloud of vapor and small particles can be seen around the principal particle. In the third, the particle is hitting the edge of a lead target.)**

## SHADOWGRAPH SYSTEM

Photographing small particles from the exploding-foil gun is complicated by the dense radiating plasma surrounding the particle in the free-flight region. We have found that we can discriminate against this plasma, however, by using an intense pulsed back-lighting source to penetrate the plasma and illuminate the solid particle. Before showing the results of recent tests, we will review the methods that are presently being used.

A schematic diagram of the backlighting arrangement is shown in Figure 19. This basic arrangement is used with the streak camera or the double-pulsed Kerr cell camera.

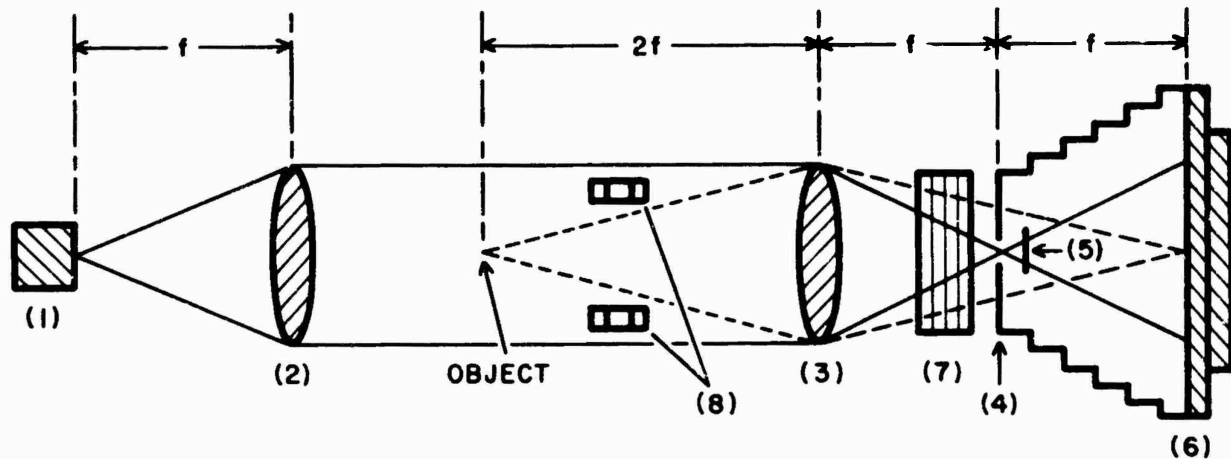


Figure 19. Optical System for Shadow Photography

The optical system consists of a high-intensity point light source, an Aero Ektar  $f/2.5$  7-in. collimating lens, and  $f/5.6$  15-in. achromatic objective lens, a telecentric stop, a filter holder, and a film holder. The light source is imaged at a telecentric stop which allows all the collimated light to reach the film plane. Of the light originating at the object plane, however, only that which is parallel to the optical axis passes through the telecentric stop, and most of the light from the object plane is eliminated.

For the double-pulsed Kerr cell camera, a Kerr cell shutter is inserted (7). This shutter opens twice and passes light for a preselected time interval (10 to 20 nsec each time) with a preselected time interval between openings. The pulsed light source (1) is also a double flash, and it is timed to reach peak intensity simultaneously with the opening of the Kerr cell shutter. The duration of the light flash is about 50 times the interval that the shutter is open. The film (7) is stationary, and two pictures are superimposed on one piece of film.

### DOUBLE-PULSED KERR CELL CAMERA

This camera will use a single Kerr cell shutter to take two pictures superimposed on the same film. The Kerr cell will be subjected to two voltage pulses with a variable time interval between pulses.

One method of double-pulsing a Kerr cell is shown in Figure 20. Initially,  $C_1$  is charged through  $R_1$  and  $R_2$  to the voltage required to fully open the Kerr cell, which in the case of the Electro-Optical cell is 35 kV. Application of a trigger pulse to  $V_1$  will suddenly charge the transmission  $TL_1$  line producing a 35 kV square-wave pulse across the Kerr cell. The duration of this pulse is determined by the total length,  $\ell$ , of the transmission line and can be made as short as 5 nsec. A second pulse will be applied to the Kerr cell when  $TL_1$  is discharged by application of a trigger pulse to  $V_2$ . This trigger pulse is formed at the time  $TL_2$  is discharged by  $V_1$  and is delayed by a pre-determined amount by a delay line  $DL_1$ , consisting of a length of RG 65/U delay cable (0.042  $\mu$ sec/ft). Interframe time can be varied from several nsec to several  $\mu$ sec by varying the length of  $DL_1$ . We will discuss the Kerr cell camera in detail when the camera has become operational.

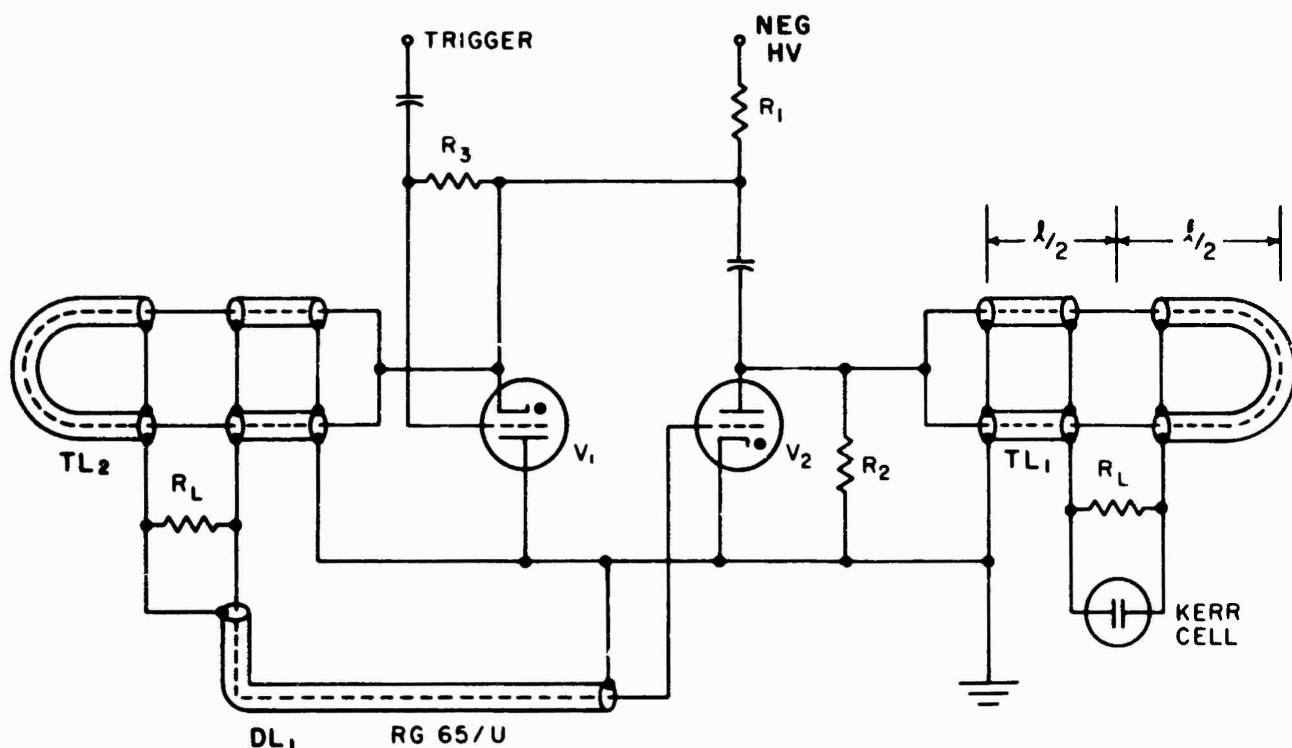


Figure 20. Schematic Diagram of Circuit for Double-Pulsing a Kerr Cell Shutter

### STREAK-FRAMING PHOTOGRAPHY

A different type of pulsed light source (1) is employed when the optical system shown in Figure 19 is used for streak-framing photography. The pulse duration and effective exposure time is adjusted such that it exceeds the particle transit time across the field by about a factor of 2. Dovetail prisms (8) are inserted in the collimated light region. The Kerr cell shutter (7) is replaced by a mechanical capping shutter, and the film plane (6) becomes the entrance slit of the streak camera.

Since the use of the streak camera to take simultaneous streak and framing pictures involves a complicated geometry, we will use Figures 21 and 22 to explain its operation.

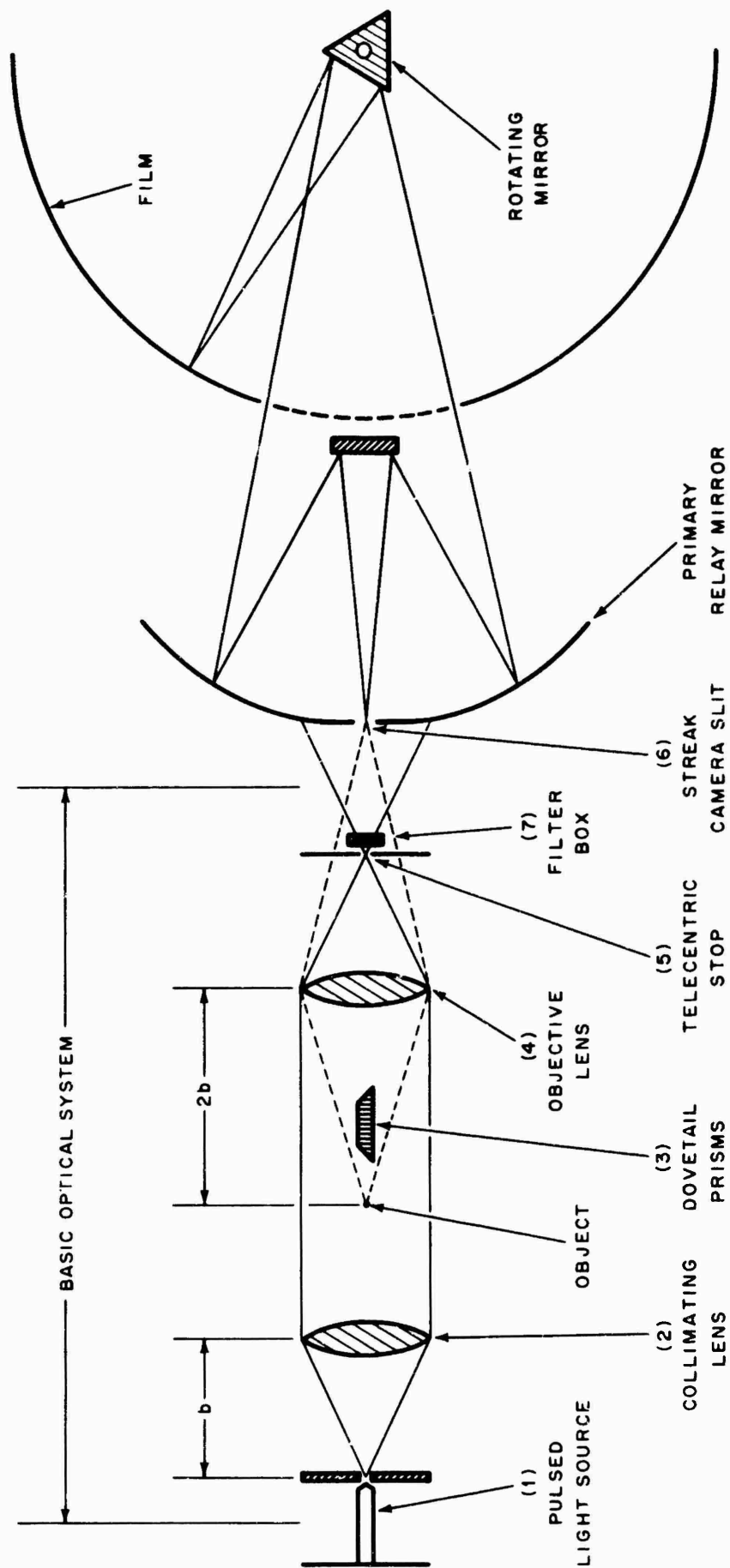


Figure 21. Schematic Diagram of Basic Optical System Modified for Use with Streak Camera

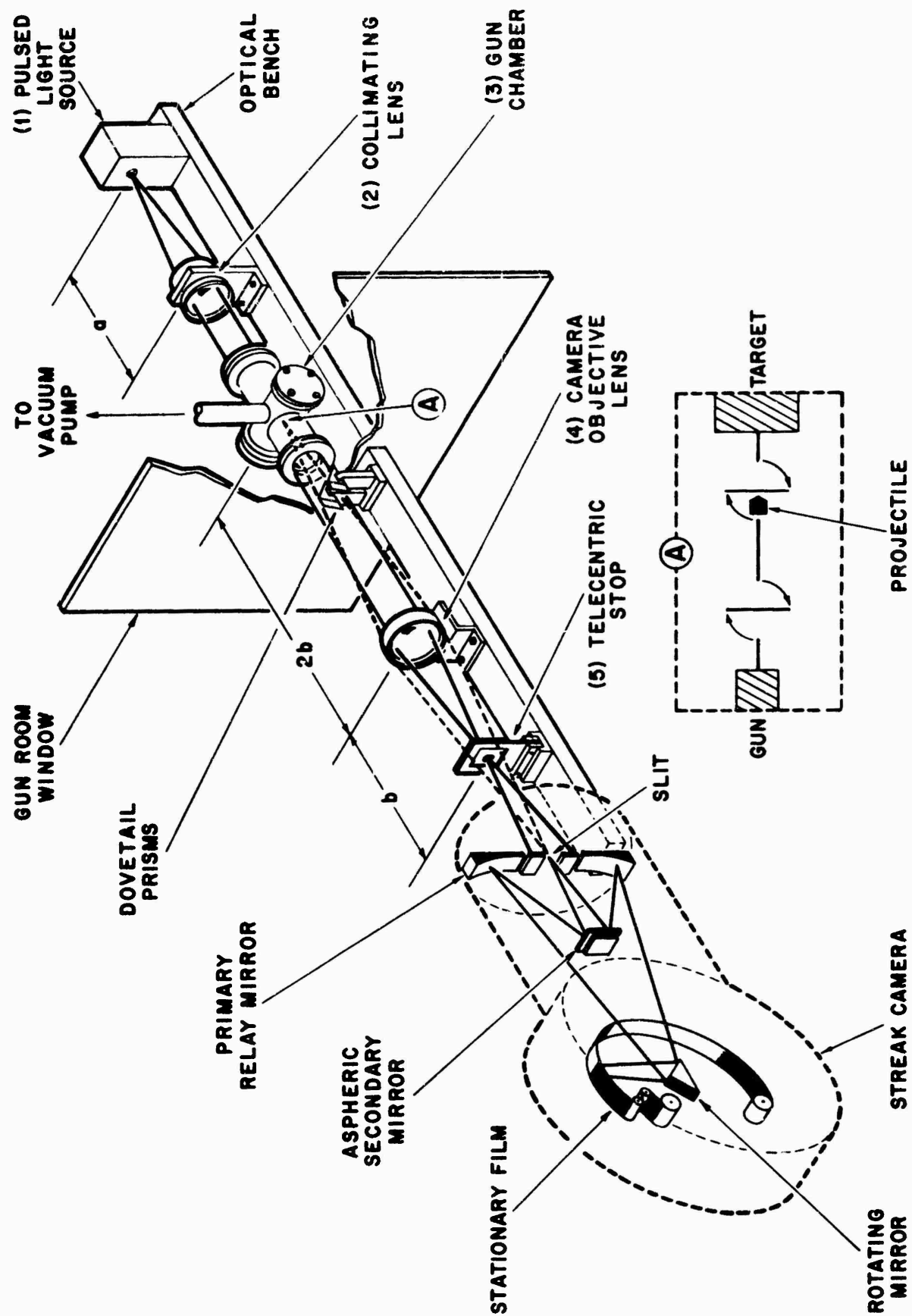


Figure 22. Method of Measuring Particle Velocity

Figure 21 shows a schematic diagram of the basic optical system and streak camera. As indicated above, the object plane is imaged on the slit of the streak camera, which has its regular objective lens replaced by the second lens (see (4) in Figure 21) of the basic optical system. In operation, an image of the slit is focused on the stationary film of the camera by its internal-relay optical system. The light beam is reflected onto the film by a prism-shaped mirror that rotates at high speed. The rotation of the mirror sweeps the slit image along the stationary film at a speed determined by the rate of mirror rotation and the length of the rotated beam. When the turbine rotates at a speed of 2500 rps, the image sweeps at a rate of  $0.9 \text{ cm}/\mu\text{sec}$  on the film. Minimum slit width is approximately  $5 \times 10^{-3} \text{ cm}$ . The internal relay optics have a magnification of 0.5. The time resolution of the camera is the time required to sweep one slit width on the film, or  $3 \times 10^{-9} \text{ sec}$ . Any displacement that occurs along the front slit of the streak camera is swept as a continuous function of time along the film in the camera. The camera therefore records displacement in one dimension as a continuous function of time.

To take simultaneous streak and framing pictures that are also backlighted, several changes are made to the arrangement described above (see Figure 22). Photographing with a streak camera requires the insertion of dovetail prisms into the optical system. When set at the proper angle, these prisms rotate part of the image on the camera slit plane. This rotation of the object relative to the slit at the camera slit plane can be thought of as rotating a section of the projected slit image at the object plane, as indicated by inset A in Figure 22. Figure 23 illustrates how the picture is taken. Here we show the projected slit image (dotted line) at the object plane; the gun, particle trajectory, and target are also shown at this plane.

When the particle moves along the trajectory from A to B (see Figure 23), a shadow streak is traced on the film A' to B'. When the particle travels from B to C, it crosses the rotated section of slit and traces its image on the film B' to C'. A similar image is traced on the film between D' and E' when the particle travels between D and E. Streak shadows are recorded on the film C' to D' and E' to F' as the particle follows the trajectory from C to D and E to F. If the impact results in the splash of dense material from the target, a shadow will be noticeable on the film F' to G'. Using this method, one can insert additional dovetail prisms and obtain one frame for each one inserted. The number of prisms that can be thus inserted is limited by the physical size of the particle to be observed and by the magnification of the optical system. For small particles or for low magnification, smaller dovetail prisms could be used and six or twelve frames could easily be obtained. If additional pictures were required, some sacrifice would have to be made in the length of streak record. For our present program, two frames with a good streak record are adequate.

Another slight modification to the conventional photographic arrangement is required to take backlighted streak pictures with the Beckman & Whitley Model 339B streak camera. In normal use, the internal relay optics of the camera are arranged such that light from the primary relay mirror to the rotating mirror passes to one side of the film holder. With the optical arrangement shown in Figure 22, this is possible only if one quarter of the area of the primary relay mirror is used and the camera is angled for alignment. This slightly changes the effective f-number of the system.

The effective exposure time for taking pictures this way is the time that it takes the image to move one slit width on the film. For a slit width of  $5 \times 10^{-3} \text{ cm}$ , this is  $3 \times 10^{-9} \text{ sec}$ . However, if the particle image on the film is traveling at the same speed

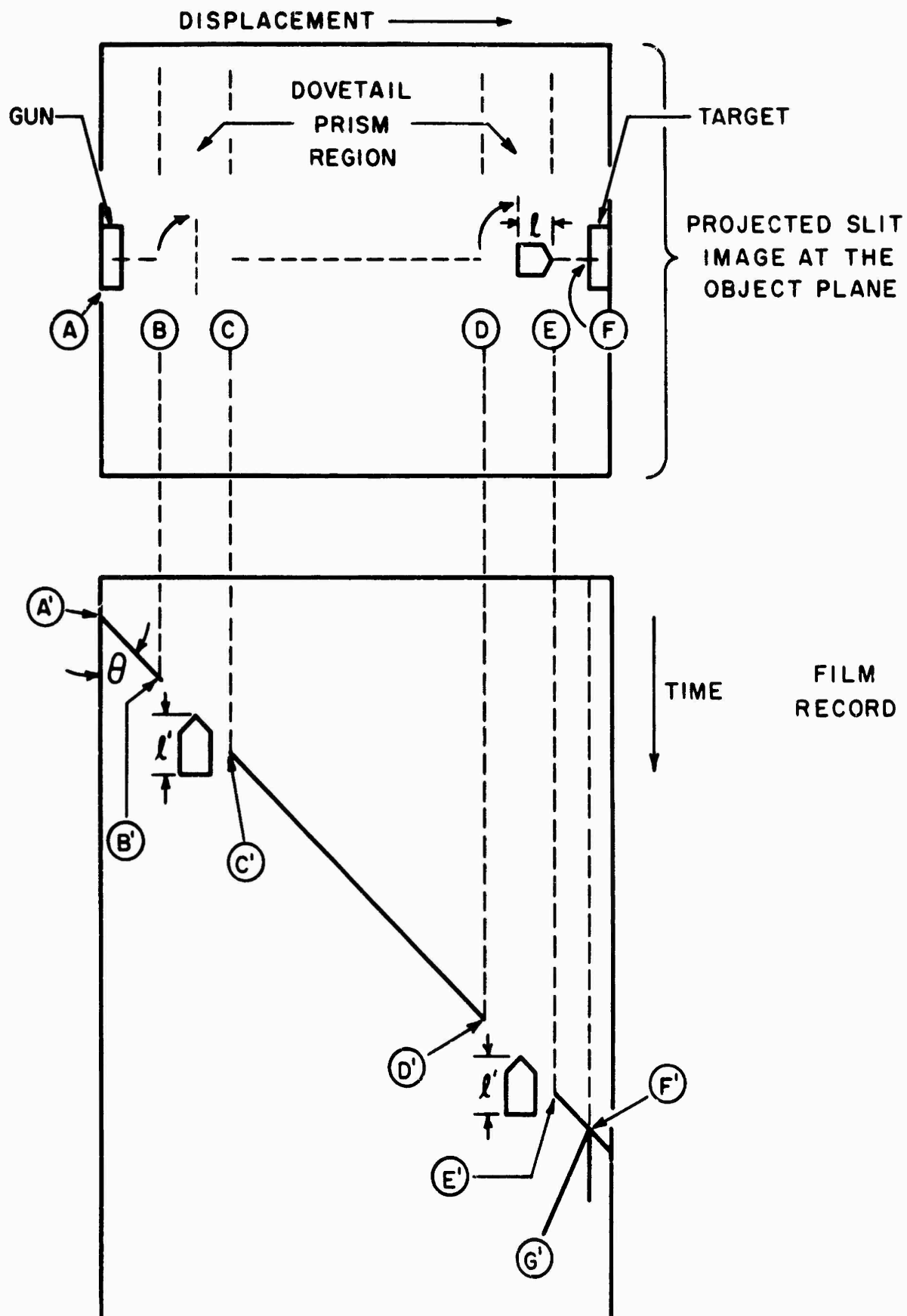


**Figure 23. Method of Taking Velocity Synchronized Streak Picture**

as the camera writing speed, they are "velocity-synchronized"\* with no relative motion. Therefore, the picture quality is improved even more than the exposure time would indicate. The image is "velocity-synchronized" when the angle  $\Theta$  (Figure 23) is equal to  $45^\circ$ . If the image is not "velocity-synchronized," the image size will be expanded ( $\Theta < 45^\circ$ ) or contracted ( $\Theta > 45^\circ$ ) along the time axis. That is, dimension  $l$  (Figure 23) is equal to  $l'$  if  $\Theta = 45^\circ$  and  $l$  is smaller than  $l'$  if  $\Theta < 45^\circ$ .

Figure 24 is a picture of our laboratory installation of the basic optical system used with the streak camera. The system is mounted over one capacitor bank.

In Figure 25 we show four streak-framed photographs of particles in flight.



Figure 24. Laboratory Installation of Optical System Used with Streak Camera

### MEASUREMENT OF PARTICLE MOMENTUM

To determine the impacting mass of a particle fired in our gun, momentum-transfer measurements must be made, since it is impossible to weigh the actual particle either before or after the shot. In our standard projection technique, a disc-shaped particle the same size as the "gun barrel" is punched out of a Mylar diaphragm of uniform thickness. After a shot, a disc-shaped hole is found in the recovered remnant of the larger piece, and the uniformity of the impact indicates that the explosion breaks out a single, uniform, disc-shaped particle. However, during the few microseconds that the disc is accelerated, it is subject to extreme temperature gradients and "barrel friction," and it is reasonable to expect that some ablation could take place early in the acceleration phase. To determine the extent of any possible particle mass losses, a method of measuring the momentum transfer of the particle has been implemented.

---

\*The idea of "velocity synchronization" was suggested by T. Holland, Beckman & Whitley, Inc.





a. Taken at 23,800 ft/sec  
Particle 1/8-in. diam 0.010-in. thick Mylar



b. Taken at 26,500 ft/sec  
Particle 1/8-in. diam 0.010-in. thick Mylar



c. Taken at 20,000 ft/sec  
Particle 3/16-in. diam 0.010-in. thick Mylar



d. Taken at 23,000 ft/sec  
Particle 1/4-in. diam 0.010-in. thick Mylar

Figure 25. Streak Framing Pictures of Particles in Flight

It had been suggested that this momentum might be measured with a ballistic pendulum, but when the difficulties involved in data measurement, compensation for background, and late time effects peculiar to this gun were evaluated, the more direct technique of measuring target-recoil velocity was chosen. A primary consideration in this choice was the necessity to eliminate the air inrush caused by the breakdown of the vacuum in the gun chamber after each shot. The reaction time for a ballistic pendulum is longer than the time it takes the air inrush to reach the target ( $\approx 10$ -20 msec), and the only way to eliminate these air effects is to enclose the entire operation in a fairly large vacuum chamber. Such a facility modification was not practical for this contract, and with a properly designed target-recoil system, air inrush is not serious. A fast-rising ( $< 5 \mu\text{sec}$ ), short-duration ( $\approx 5$  msec) target backlighting source completely eliminates this effect from the experiment.

At the present time, particle mass is determined from the momentum transfer equation in the form

$$m = \frac{MV}{v}$$

where

$m$  = particle mass

$M$  = the weighed target mass

$V$  = the target velocity measured from framing camera picture

$v$  = the incident particle velocity measured from streak pictures.

In this form no effort is made to compensate for target mass losses, or the initial explosive reaction occurring when the particle first enters the target. These effects are small and very difficult to evaluate exactly, but any correction for them would reduce the calculated particle mass by some small and near constant factor.

To assure that propellant plasma and other debris were not affecting the measurement, "background" shots were fired. The guns were identical in all respects with those used in shots described above, but no particle was loaded into the gun. In all cases, the momentum of the plasma was lower than that of the particle by a factor of 10, although the plasma velocities were 2 to 3 times faster than the highest particle velocities.

The method chosen for the target recoil studies features a low density target designed to trap the momentum of a particle of a given mass and velocity. This target design (see Figure 26) uses a very light canister that is filled with a predetermined number of thin aluminum sheets (0.005 in.  $\rightarrow$  0.010 in.) and relatively thick Styrofoam absorbers. The weight of these targets can be varied from 1 to 20 g as the particle material and velocity range is changed.

The open end of the target is covered with a thin foil Mylar laminate (0.003 in. total thickness) that allows the particle to enter the target easily but is strong enough to eliminate target-mass losses during impact and to trap any recoil momentum (except for that

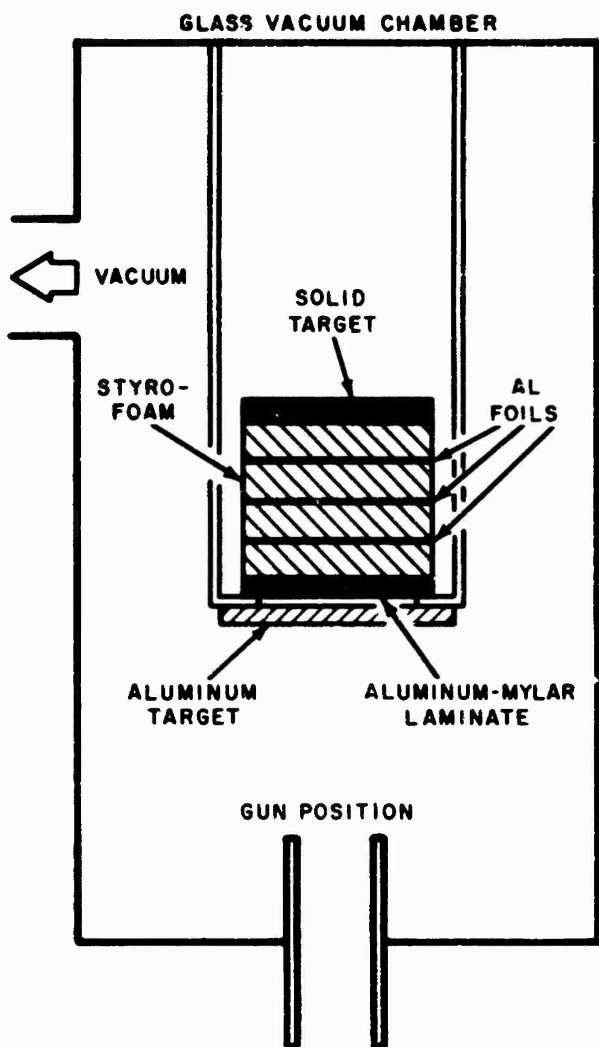


Figure 26. Target Recoil Configuration

lost out the small hole through which the particle enters) resulting from flash vaporization and hydrodynamic blowoff. At each interface the particle loses some mass as vapor and small fragments, and these are captured by the absorbing material.

By this technique, the normal momentum is conserved without introducing additional accelerations. Measurements are taken in the vertical direction in less than 2 msec over distances of about 2 cm. The target velocities are measured with a Beckman & Whitley Dynafax framing camera, which can take 224 well-resolved data frames in times as short as 9 msec (see Figure 27). For analysis, each frame is magnified 20 times, and 98% accuracy is possible in target velocity determination.

During the contract period, a substantial quantity of data was taken by the target recoil method described above. However, particle mass determination depends directly upon the measurement of particle velocity. Earlier in this chapter we described the improvements that have been made in the measurement of particle velocity. Since these improvements were made, we have not taken any target recoil data. Therefore, we now consider all of the target recoil data previously taken as preliminary, and they are therefore not included in this report.

## ELECTRICAL MEASUREMENTS

The exploding-foil gun is a very complicated load transducer. Therefore, a knowledge of the electrical input to the gun is very important to an understanding of its operation.

The current through the gun is measured by a very low inductance, single turn transformer mounted on the electrical lead to the gun. The  $dI/dt$  signal generated in the loop is electrically integrated, and displayed on a Tektronix Model 551 oscilloscope. The voltage signal displayed on the oscilloscope is proportional to current in the gun circuit to a maximum deviation of 5% over the frequency range 50 kc to 15 Mc (the limit of the scope amplifier). This has been verified by careful frequency response measurements.

To calibrate the current measuring system, the exploding-foil gun is replaced by a short circuit load. The system is charged to a known potential and discharged. The current calibration is then obtained from an analysis of the oscilloscope trace that is obtained during this calibration test.

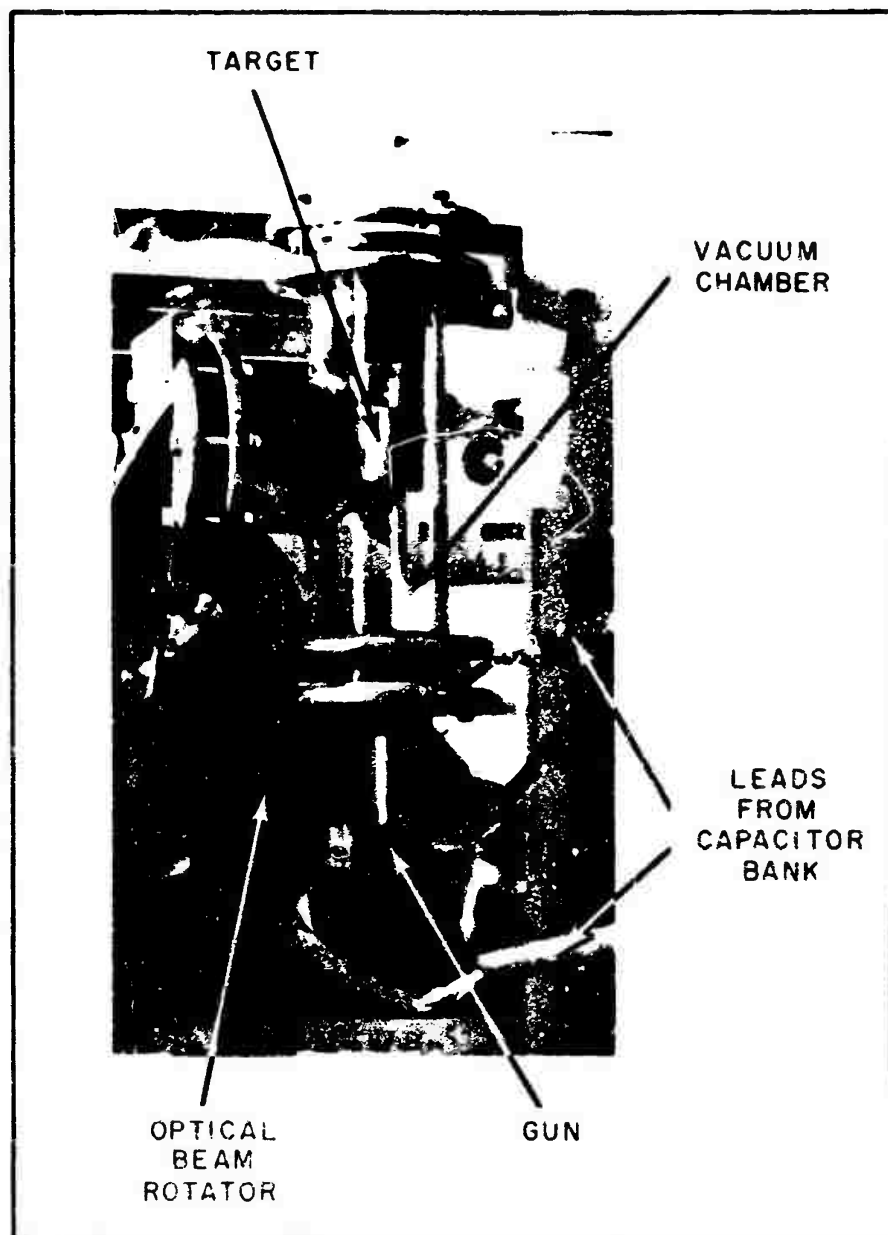


Figure 27. Gun and Target Chamber for Recoil Studies

We assume that the discharge circuit inductance is constant. This is approximately true for triggered switches firing at relatively low ambient pressure. The circuit resistance must also be constant over the time interval used for the calibration.

The discharge current in the oscillatory RLC circuit ( $R^2C^2 < 4LC$ ) is described by

$$I = \frac{2Q_0 e^{-(R/2L)t} \sin \beta t}{\sqrt{4LC - R^2C^2}} \quad (1)$$

where

- $Q_0$  = the initial charge on the capacitor
- $R$  = total circuit resistance
- $L$  = total circuit inductance
- $\beta$  =  $2\pi \times$  discharge frequency
- $C$  = total circuit capacity.

$Q_0$  is determined from the initial charge on the capacitor:

$$Q_0 = CV_0.$$

$L$  is estimated from the discharge frequency of the electrical circuit

$$L = \frac{1}{4\pi^2 f^2 C}.$$

$C$  and  $f$  are measured.

$R$ , the total circuit resistance, is obtained from the logarithmic decrement of the electrical signal

$$R = \frac{2L}{t_2 - t_1} \ln \frac{i_1}{i_2} ;$$

$i_1$  and  $i_2$  are the magnitude of successive current peaks, and  $t_1$  and  $t_2$  are the corresponding times.

Total circuit resistance,  $R$ , is evaluated for each set of successive current peaks. A time is selected for which  $R$  is approximately constant for two time intervals. If difficulty is encountered in finding such a time, the calibration is best carried out by using a low voltage source (300 V) and a good manual switch in place of the triggered air gap switch. Then  $R$  is very small and

$$e^{-(R/2L)t} \approx 0.$$

and Eq. (1) becomes

$$I = \frac{Q_0 \sin \beta t}{\sqrt{LC}}. \quad (2)$$

The potential across the gun is measured as a function of time by means of the circuit shown in Figure 28. Two resistive dividers  $R_1 R_2$  and  $R'_1 R'_2$  are connected from either side of the gun to ground. The dividers are constructed of a string of 2-watt

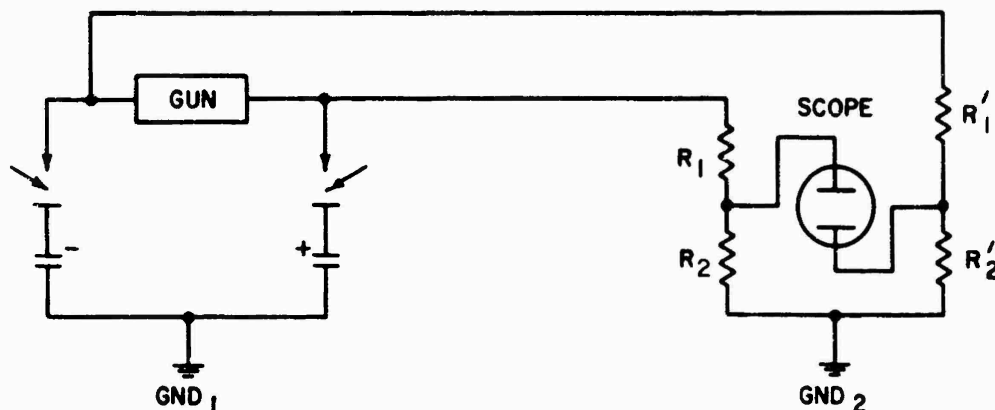


Figure 28. Schematic Diagram of Electrical Circuit Used for Measurement of Potential Across the Gun

Allen Bradley low inductance carbon resistors. The resistors are potted in lucite tubes and mounted in a copper shielded container. Two, very short, unshielded leads are extended to the main capacitor discharge circuit.

The resistive dividers feed a 50-ohm shielded transmission line to the oscilloscope. The two signals are fed into the two inputs of a Tektronix type G differential amplifier.

The frequency response of this divider system was checked and found to vary  $\pm 5\%$  for frequencies between 50 kc and 4 Mc.

The use of resistive dividers with an energy storage system of the type shown in Figure 28 poses some operational problems but is satisfactory when care is taken. If one of the switches, SW-1 or SW-2, should fire before the other or if the circuit should open up at the gun position, then one of the capacitors,  $C_1$  or  $C_2$ , would discharge through a resistive divider, depositing all of its energy into the divider. This is sufficient energy to blow up the divider.

Figure 29 shows the results of electrical measurements for a typical shot. Current, potential, and energy deposited in the gun are all plotted on the same time scale as a streak picture that was taken of the event. The electrical energy deposited before the beginning of particle acceleration is noted in the figure.

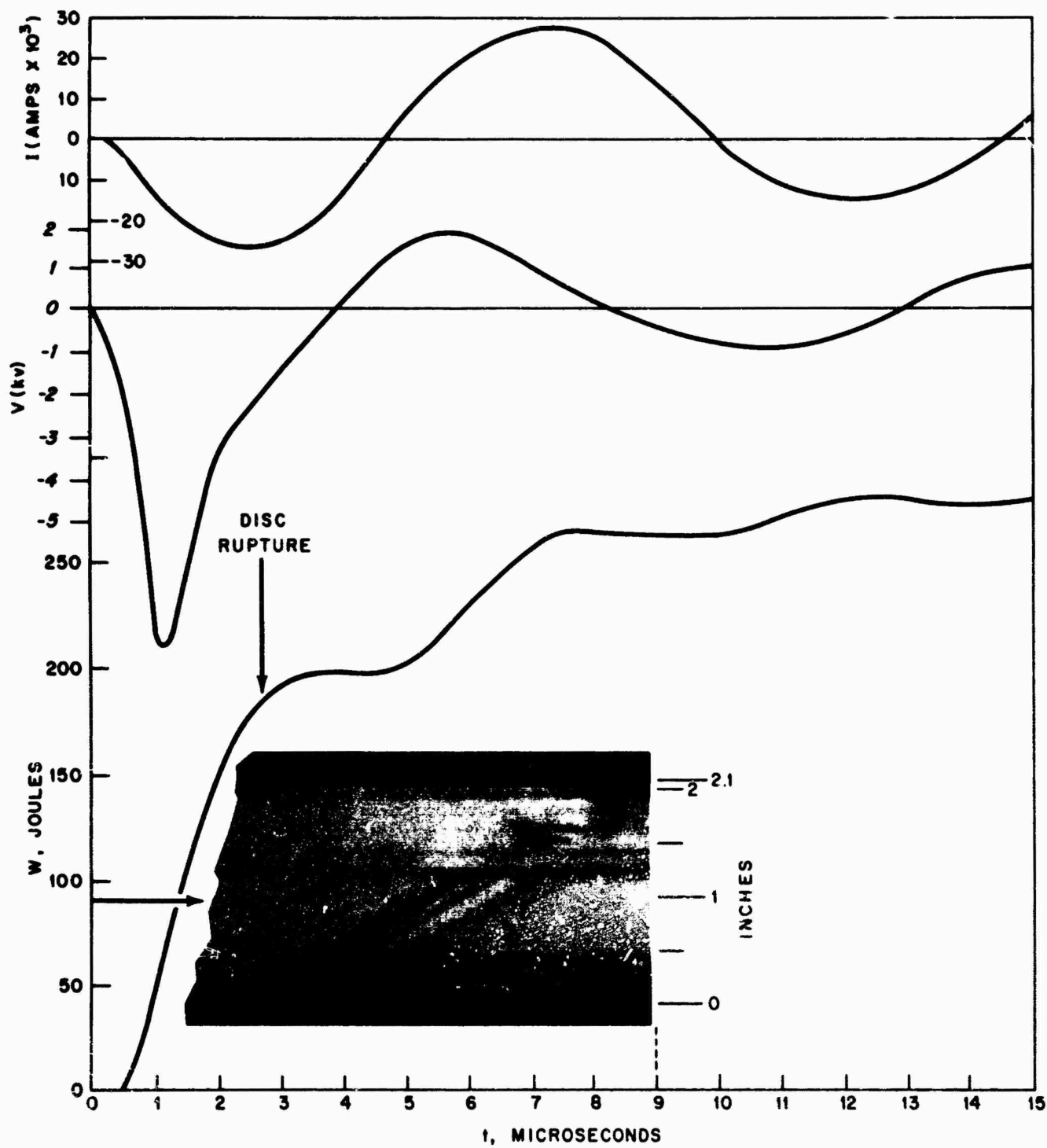


Figure 29. Pictorial Correlation of Electrical and Photographic Measurements

## CHAPTER 5

### THEORETICAL STUDY OF IMPACT OF DISC-SHAPED PARTICLES

During the first part of the research effort, according to the measurements that were taken then, we believed that our 0.25-in. diameter flat disc particles were impacting the targets flat, and at velocities up to 50,000 ft/sec. The assumption that the particles impacted flat was reasonable, since we had no pictures to prove otherwise, and since orientation is normally a stable one in uniform gas flow. For this reason, we carried out an extensive theoretical analysis to explain the experimental data that we obtained and to guide future experimental work. Later, when refined diagnostic techniques were available, we found experimental errors in the measurement of mass and velocity. Therefore, we cannot now publish that part of the theoretical work pertaining to the experimental data. However, that portion of the theory which was intended to guide the experimental work is still useful, and we therefore present it in this chapter along with recommendations for continuing a theoretical program.

#### PRELIMINARY CALCULATIONS

The thin disc shape of the particle makes it easy to calculate the initial impact. We simply perform a one-dimensional shock analysis on the impact of two plates. The results of this calculation will tell us the state of the particle and target a short time after impact and will indicate the type of theory to apply for subsequent analysis of the cratering.

#### INITIAL IMPACT CALCULATIONS

We will consider here the impact of aluminum and copper particles on lead targets (see Figure 30). First, we will set up the equations governing the impact of two infinite flat plates of dissimilar materials. The relative velocity of impact,  $v_0$ , will be along a line perpendicular to the planes. Referring to Figure 31, we may write a set of Rankine-Hugoniot relations across shocks 1 and 3.

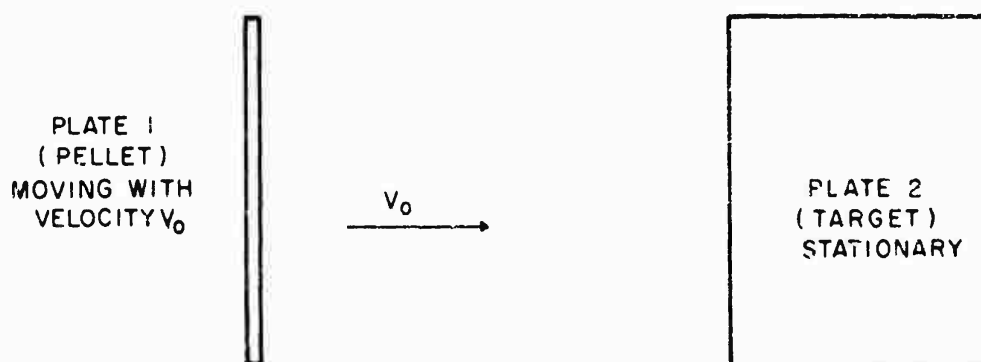


Figure 30. Plates Before Impact



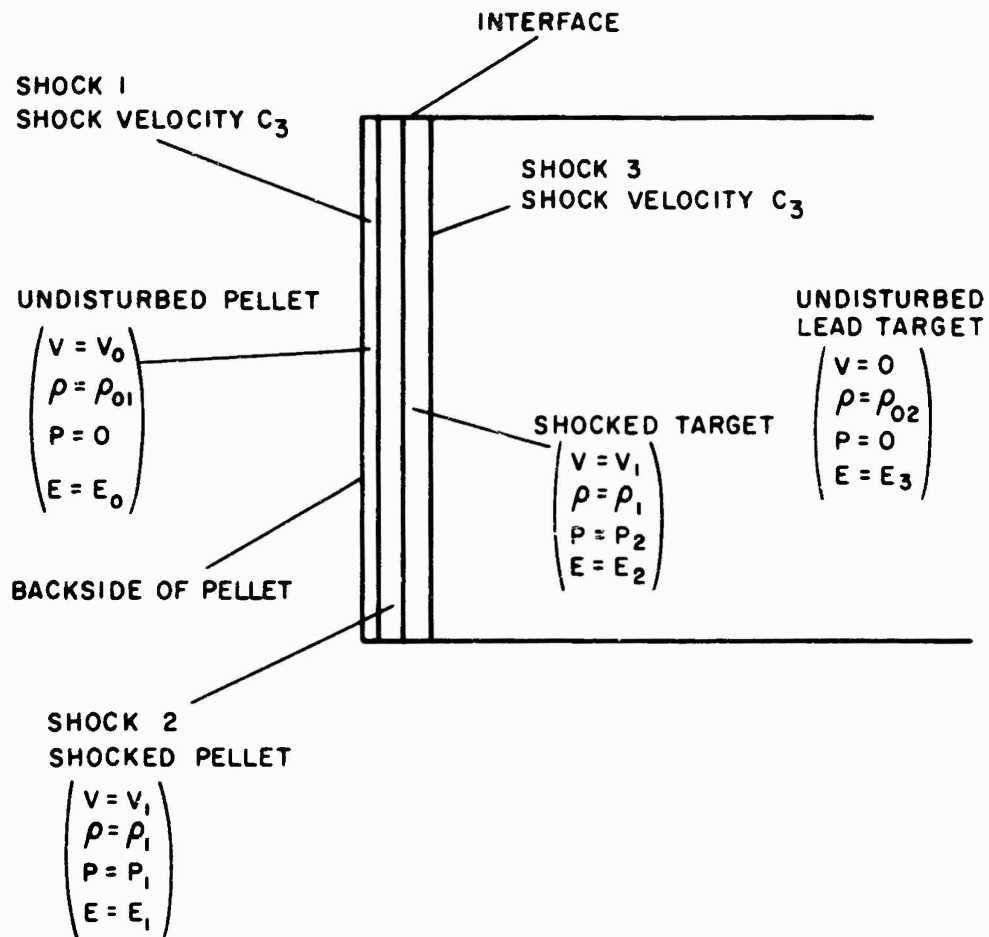


Figure 31. Plates After Impact

In a frame in which shock 1 is stationary, the Rankine-Hugoniot relations across shock 1 are:

$$(v_0 + c_1) \rho_{01} = (v_1 + c_1) \rho_1$$

$$p_1 = \rho_0 (v_0 + c_1)^2 - \rho_1 (v_1 + c_1)^2 \quad (3)$$

$$\frac{(v_0 + c_1)^2}{2} + E_0 = \frac{(v_1 + c_1)^2}{2} + \frac{p_1}{\rho_1} + E_1.$$

where

- E = internal energy
- v = mass velocity
- c = shock velocity
- $\rho$  = mass density
- p = specific pressure.

Subscripts are explained in Figure 31.

Similarly, the Rankine-Hugoniot relations associated with shock 3 are:

$$\begin{aligned}
 c_3 \rho_{o2} &= (c_3 - v_1) \rho_2 \\
 p_1 &= -\rho_2 (c_3 - v_1)^2 + \rho_o c_3^2 \\
 \frac{(c_3 - v_1)^2}{2} + \frac{p_2}{\rho_2} + E_2 &= \frac{c_3^2}{2} + E_3 .
 \end{aligned}
 \tag{4}$$

These equations may be manipulated to yield:

$$\begin{aligned}
 E_1 - E_o &= \frac{p_1}{2} \left[ \frac{1}{\rho_{o1}} - \frac{1}{\rho_1} \right] \\
 E_2 - E_3 &= \frac{p_1}{2} \left[ \frac{1}{\rho_{o2}} - \frac{1}{\rho_2} \right] \\
 E_1 - E_o &= \frac{1}{2} (v_o - v_1)^2 \\
 E_2 - E_3 &= \frac{1}{2} v_1^2 .
 \end{aligned}
 \tag{5}$$

These equations may be solved if we know two further equations of state of the form:

$$\begin{aligned}
 E_1 - E_o &= f_1(p_1, \rho_1) \\
 E_2 - E_3 &= f_2(p_2, \rho_2) .
 \end{aligned}
 \tag{6}$$

Experiments and theory have produced some curves of the form given in Eq. (6). However of more use to us are curves of the Hugoniot, that is, curves expressing the relationship between  $p$  and  $\rho$  in the disturbed part of the shock. We show such curves in Figure 32 for three materials.

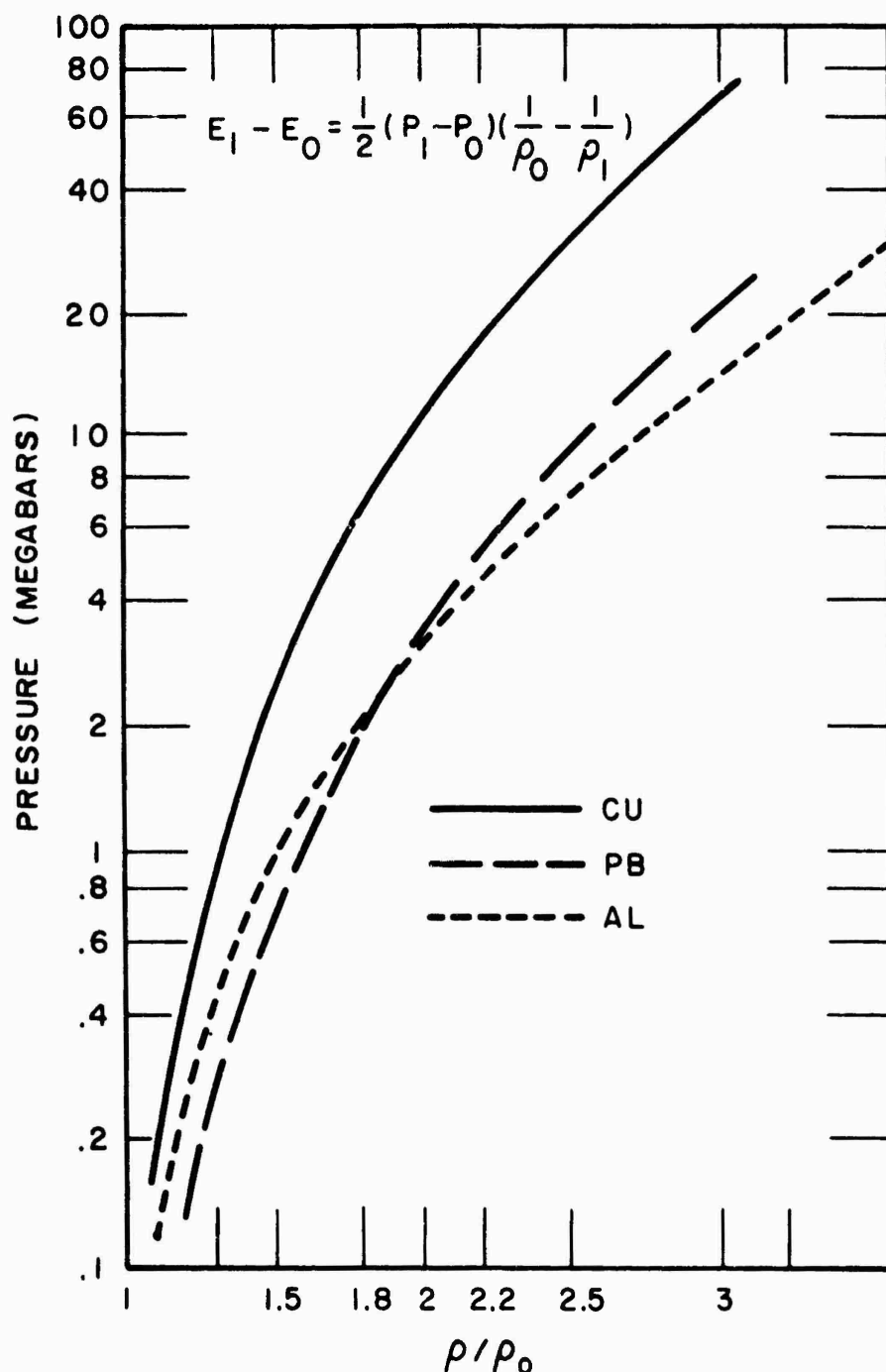


Figure 32. Hugoniot Curves for Copper, Lead, and Aluminum

These curves in conjunction with Eq. (5) may be used to solve for  $(E_1 - E_0)$ ,  $(E_2 - E_3)$ ,  $\rho$ ,  $p_1$ ,  $\rho_2$ , and  $v_1$ . We use an iteration procedure as follows. Make an assumption for  $p_1$ . Use curves on Figure 32 to find  $\rho_1$  and  $\rho_2$ . Calculate  $(E_1 - E_0)$  and

( $E_2 - E_3$ ) from Eq. (5). Then calculate  $v_1^2$  separately from each of the equations ( $E_1 - E_0$ ) =  $1/2(v_0 - v_1)^2$  and ( $E_2 - E_3$ ) =  $1/2 v_1^2$ . Compare calculated values of  $v_1$ . If they do not agree, adjust  $p_1$  and repeat procedure. Continue procedure until satisfactory agreement is obtained.

In Table 1 we give the results of such a calculation for an aluminum particle impinging upon a lead target. We took  $\rho_{01} = 2.7$  g/cc and  $\rho_{02} = 11.4$  g/cc.

TABLE 1  
ENERGY, PRESSURE, AND DENSITY INFORMATION FOR  
ONE-DIMENSIONAL ALUMINUM-LEAD IMPACTS

$v_0$ (cm/sec)	$v_1$ (cm/sec)	( $E_1 - E_0$ ) (Joules/g)	( $E_2 - E_3$ ) (Joules/g)	$p$ (dynes/cm <sup>2</sup> )	$\rho_1/\rho_{01}$	$\rho_2/\rho$
$2 \times 10^5$ (6,600 ft/sec)	$0.72 \times 10^5$	820	260	$2.55 \times 10^{11}$	1.21	1.31
$4 \times 10^5$ (13,300 ft/sec)	$1.4 \times 10^5$	3,380	980	$6.4 \times 10^{11}$	1.4	1.51
$6 \times 10^5$ (19,900 ft/sec)	$2 \times 10^5$	8,000	2,000	$1.1 \times 10^{12}$	1.6	1.7
$10^6$ (33,100 ft/sec)	$3.3 \times 10^5$	22,500	5,450	$2.54 \times 10^{12}$	1.91	1.97
$2 \times 10^6$ (66,000 ft/sec)	$6.5 \times 10^5$	91,000	21,000	$8.1 \times 10^{12}$	2.6	2.4
$4 \times 10^6$ (133,000 ft/sec)	$1.33 \times 10^6$	355,000	82,000	$2.7 \times 10^{13}$	3.5	3.2

It is also useful to know the shock speeds  $c_1$  and  $c_3$ , and we present in Table 2  $c_1$ ,  $c_3$ ,  $v_1 + c_1$ , and  $c_3 - v_1$  as a function of  $v_0$ .

The high pressures and energy densities given in Table 1 indicate that, initially, the particle-target system influenced by the impact will behave like a fluid. There are no data at these high densities to show definitely that the material has no significant strength capability, but at pressures of over 3,000,000 lb/in.<sup>2</sup> we would not expect it to possess such capability. Though we have not made detailed calculations for a copper-lead impact, rough calculations show that similar high pressures and energy densities will be obtained.

TABLE 2  
VELOCITY INFORMATION FOR  
ONE-DIMENSIONAL ALUMINUM-LEAD IMPACTS  
(Velocities cm/sec)

$v_0$	$c_1$	$c_1 + v_1$	$c_3$	$c_3 - v_1$
$2 \times 10^5$	$5.5 \times 10^5$	$6.1 \times 10^5$	$3 \times 10^5$	$2.3 \times 10^5$
$4 \times 10^5$	$5.1 \times 10^5$	$6.5 \times 10^5$	$4.2 \times 10^5$	$2.8 \times 10^5$
$6 \times 10^5$	$4.6 \times 10^5$	$6.6 \times 10^5$	$4.9 \times 10^5$	$2.9 \times 10^5$
$1 \times 10^6$	$4.1 \times 10^5$	$7.4 \times 10^5$	$6.7 \times 10^5$	$3.4 \times 10^5$
$2 \times 10^6$	$1.9 \times 10^5$	$8.4 \times 10^5$	$1.11 \times 10^6$	$4.6 \times 10^5$
$4 \times 10^6$	$-2.8 \times 10^5$	$1.05 \times 10^6$	$1.93 \times 10^6$	$6.0 \times 10^5$

### ENERGY DISTRIBUTION IN PARTICLE AND TARGET WHEN SHOCK 1 REACHES BACK SURFACE OF PARTICLE

The shocks will progress undisturbed until the shock  $c_1$  encounters the back edge of the particle. At this time the whole particle will be moving with velocity  $v_1$ . In a coordinate system moving with velocity  $v_1$ , the particle, which is now a liquid or gas, will expand away from this target. We will consider this effect below. To investigate the applicability of previous theories, we will calculate here the state of the particle and target when shock 1 reaches the back end of the particle. We summarize in Table 3 the condition of particle and target for an aluminum particle, 1/4 in. in diameter and weighing 10.8 mg, impinging on a lead target. We note that the thickness of this particle is  $1.2 \times 10^{-2}$  cm. Table 3 shows that, over the whole range of interest, about two thirds of the energy is internal energy and about one third is kinetic energy. Further, the target material contains about 40% of the energy.

TABLE 3  
ENERGY DISTRIBUTION WHEN SHOCK 1 REACHES  
BACK PART OF PARTICLE\*

$v_0$ (cm/sec)	Initial Kinetic Energy of Particle (joules)	Final Kinetic Energy of Particle (joules)	Final Internal Energy of Particle (joules)	Final Kinetic Energy of Target (joules)	Final Internal Energy of Target (joules)
$2 \times 10^5$	21.6	3.0	9.2	4.7	4.7
$4 \times 10^5$	86	11	37	19	19
$6 \times 10^5$	194	22	86	42	42
$1 \times 10^6$	540	61	245	117	117
$2 \times 10^6$	2160	230	930	500	500
$4 \times 10^6$	8600	900	3700	2000	2000

\* Values were sometimes adjusted up to 10% to obtain an energy balance.

## PARTICLE EXPANSION AFTER SHOCK 1 REACHES BACK PART OF PARTICLE

There is one further calculation that can easily be made after the shock reaches the back surface of the particle if we assume that the expansion of the vapor following this time is adiabatic. We can calculate the state of the particle until the rarefaction wave propagating in the particle toward the target reaches the original particle-target interface.

We made this calculation for  $v_0 = 10^6$  cm/sec. We assumed that  $\gamma = 3$ . In a system moving with velocity  $v$ , the velocity distribution in the particle (where  $x = 0$  is the original back surface of the particle) is:

$$u = \frac{1}{2} \left( \frac{x}{t} - c_0 \right) \quad (7)$$

where

$$c_0 = \sqrt{\frac{\gamma p_1}{\rho_1}}.$$

The density is:

$$\rho = \frac{\rho_1}{2} \left[ \frac{x}{c_0 t} + 1 \right]; \quad (8)$$

$p$  and  $\rho$  are related by

$$p = p_1 \left[ \frac{\rho}{\rho_1} \right]^3.$$

Simple calculation shows that the internal energy in the particle, when the rarefaction wave (proceeding with velocity  $c_0$ ) hits the original forward side of the particle, is one half the internal energy it had when the expansion began. It can also be shown that the additional internal energy in the target is now  $v_1/c_0$  times the original internal energy in the particle, and the additional kinetic energy is one half  $v_1/c_0$  times this amount. The state of the particle-target system when the rarefaction wave returning from the back surface of the particle hits the original particle forward face is given in Table 4.

Note that Eqs. (7) and (8) show that, of the 70 joules in particle kinetic energy, about 60 joules have an absolute velocity away from the target.

We did not make calculations for other initial velocities since we could not decide on a reasonable  $\gamma$ . For  $v_0 = 10^6$  cm/sec,  $E = p/\gamma - 1$  when  $\gamma \approx 3$ , and it seems accepted in the field that  $\gamma = 3$  is a reasonable figure over a large range of dense vapor conditions. On the other hand, if we let  $\gamma = 3$  for say  $v_0 = 4 \times 10^5$  cm/sec, we must write  $E = p/\gamma - 1 + \text{constant}$  and we get nonphysical results as the vapor cools.

TABLE 4  
ENERGY DISTRIBUTION IN PARTICLE TARGET SYSTEM  
(When rarefaction wave intersects initial forward face of particle)

$v_0$ (cm/sec)	Initial Kinetic Energy of Particle (joules)	Kinetic Energy of Particle (joules)	Internal Energy of Particle (joules)	Kinetic Energy of Target (joules)	Internal Energy of Target (joules)
$10^6$	540	70	122	155	193

Though we proceeded no further for  $v_0 = 10^6$  cm/sec, calculations can be continued. However, they become more involved since the density changes at the interface. It is probably useful to do some further one-dimensional calculations showing how shock 3 slows down when the rarefaction wave reaches it. At the point we stopped, the penetration distance was only a little larger than the original particle thickness and, hence, the flow would still be one-dimensional for times when shock 3 slowed down.

#### REVIEW OF EXISTING THEORIES

The discussion thus far is indicative of the type of theory needed to explain the experimental results for flat particle impacts. We shall now turn to a review of previous theories.

For our review of existing theories, we relied on the recent compilations of Herrmann and Jones<sup>1</sup> and the Fifth Symposium on Hypervelocity Impact.<sup>2</sup> As a result of the calculations presented above, for application to high velocity data (above 20,000 ft/sec) we were able to dismiss immediately theories in which the projectile was unaffected during penetration. We then looked at various theories where the particle was in some sense seriously deformed. Herrmann and Jones<sup>1</sup> divide these theories into three classes: (1) hydrodynamic, (2) thermal penetration, and (3) explosive analogy. In the first class, projectile and shear strength are neglected, while in the second class the material is removed by melting or vaporization. Since both these classes are covered by the equations of compressible fluid dynamics, we consider them under the term "hydrodynamics." The last category of theories considers the crater to be identical with that found by an equivalent mass of high explosive detonated in contact with the surface of the target.

#### HYDRODYNAMIC THEORIES

Under hydrodynamic theories, we can, with Bjork,<sup>3</sup> write down the equations of a compressible gas and attempt to solve them. There are six equations: one continuity, three momentum, one energy, one equation of state ( $E = f(p, \rho)$ ). If the temperature is explicitly needed (if for example conduction effects are included), there must be a second equation of state  $T = f(p, \rho)$ .

Since analytical solutions of these equations in their most general forms are most difficult to obtain, many simple models have been studied. Such models, for example, have been considered by Zaid, Opik, and Birkhoff (see Herrmann and Jones<sup>1</sup>).

Unfortunately, none of these models is appropriate to our thin-disc particles. At the velocities we consider, the disc becomes completely a fluid less than a microsecond after impact. Thus, neither the partially rigid projectile of Zaid, nor the incompressible projectile of Opik is appropriate. Shape-charge theories are inappropriate for thin particles, being more appropriate for needle type targets.

Theories like Whipple's and Langton's (see Herrmann and Jones<sup>1</sup>) where a crater shape is assumed and all the particle kinetic energy goes into melting and vaporization (or just melting) will be used to consider some data we have obtained. However, as we shall show, these theories are inadequate for the range of data we have.

## EXPLOSIVE-ANALOGY THEORIES

Explosive-analogy theories like that of Stanyukovitch (see Herrmann and Jones<sup>1</sup>) have merit, since the conditions shown in Table 3 resemble the state of an explosive material when the detonation wave reaches the surface of the explosive. However, since the explosion is unconfined and since the diameter of the particle is an appreciable fraction of the diameter of the crater, such a theory must be used with some caution. We will discuss other limitations of the theory in the next section.

The numerical solution of the hydrodynamic equations, as was done by Bjork,<sup>3</sup> is probably the most satisfactory approach if detailed comparison with experiment is desired. However, even here, the equations are somewhat limited since they do not take account of the target strength when the local pressure and energy density are lowered in the later stages of the penetration. This effect is being studied by Riney<sup>4</sup> and Herrmann<sup>5</sup> by incorporating the effect into the hydrodynamic equations and then seeking numerical solutions. It is not now clear how important this effect is at very high velocities, but, as we shall show below, it may be important at moderately high velocities (6000-20,000 ft/sec).

Bjork's results cannot be used to compare with our experiments since they apply to cylinders where the diameter-to-length ratio is 1. Further, in his calculations, the target and particle are of the same material. For comparison with our data, special numerical calculations must be run.

## RECOMMENDATIONS

It is recommended that a program similar to Bjork's (but extended to allow for dissimilar materials) be used to get detailed numerical data of the cratering process and ultimate crater. Care must be taken to get the best possible equation-of-state data. If future experiments can be designed to give time-resolved data, these data could be compared with the numerical solution at all times. This certainly must be done if a good understanding of the cratering mechanism is to be gained.

We feel that there is little hope of obtaining analytical solutions or simple phenomenological models that will explain a wide class of conditions. While it is often felt that computer solutions are to be used only as a last resort, we feel that here it is important to use them to determine how much analysis beyond the solution of the usual hydrodynamic equations is necessary to explain hypervelocity impact data at all times. Once this is established, it will then be desirable to seek analytical solutions of the governing equations, perhaps aided by formulas that suggest themselves from the numerical solutions.



## REFERENCES

1. W. Herrmann and A. Jones, "Survey of Hypervelocity Impact Information," Massachusetts Institute of Technology, Aeroelastic and Structures Research Laboratory, A.S.R.L. Report No. 99-1 (September, 1961).
2. J. S. Rinehart, "Proceedings of Fifth Symposium on Hypervelocity Impact," Vol. I, Part 2 (April, 1962).
3. R. Bjork, "Proceedings of the Third Symposium on Hypervelocity Impact," Vol. II (February, 1959).
4. T. D. Riney, "Theory of High Speed Impact," Air Proving Ground Center, Report No. APGC-TDR-62-20 (March, 1962).
5. W. Herrmann, Private Communication.